

# Accuracy and precision of gravitational-wave models of inspiraling neutron star – black hole binaries with spin: comparison with numerical relativity in the low-frequency regime

Prayush Kumar,<sup>1,2,\*</sup> Kevin Barkett,<sup>3</sup> Swetha Bhagwat,<sup>1</sup> Nousha Afshari,<sup>4</sup>  
Duncan A. Brown,<sup>1</sup> Geoffrey Lovelace,<sup>4</sup> Mark A. Scheel,<sup>3</sup> and Béla Szilágyi<sup>3</sup>

<sup>1</sup>*Department of Physics, Syracuse University, Syracuse, NY 13244, USA*

<sup>2</sup>*Canadian Institute for Theoretical Astrophysics, University of Toronto, Toronto, ON M5S 3H8, Canada*

<sup>3</sup>*Theoretical Astrophysics 350-17, California Institute of Technology, Pasadena, California 91125, USA*

<sup>4</sup>*Gravitational Wave Physics and Astronomy Center, California State University Fullerton, Fullerton, California 92834, USA*

(Dated: February 16, 2022)

Coalescing binaries of neutron stars and black holes are one of the most important sources of gravitational waves for the upcoming network of ground based detectors. Detection and extraction of astrophysical information from gravitational-wave signals requires accurate waveform models. The Effective-One-Body and other phenomenological models interpolate between analytic results and numerical relativity simulations, that typically span  $\mathcal{O}(10)$  orbits before coalescence. In this paper we study the faithfulness of these models for neutron star - black hole binaries. We investigate their accuracy using new NR simulations that span 36 – 88 orbits, with mass-ratios  $q$  and black hole spins  $\chi_{\text{BH}}$  of  $(q, \chi_{\text{BH}}) = (7, \pm 0.4), (7, \pm 0.6),$  and  $(5, -0.9)$ . We find that: (i) the recently published SEOBNRv1 and SEOBNRv2 models of the Effective-One-Body family disagree with each other (mismatches of a few percent) for black hole spins  $\chi_{\text{BH}} \geq 0.5$  or  $\chi_{\text{BH}} \leq -0.3$ , with waveform mismatch accumulating during *early* inspiral; (ii) comparison with numerical waveforms indicate that this disagreement is due to phasing errors of SEOBNRv1, with SEOBNRv2 in good agreement with all of our simulations; (iii) Phenomenological waveforms agree with SEOBNRv2 only for comparable-mass low-spin binaries, with overlaps below 0.7 elsewhere in the neutron star - black hole binary parameter space; (iv) comparison with numerical waveforms shows that most of this model's dephasing accumulates near the frequency interval where it switches to a phenomenological phasing prescription; and finally (v) both SEOBNR and post-Newtonian models are effectual for neutron star - black hole systems, but post-Newtonian waveforms will give a significant bias in parameter recovery. Our results suggest that future gravitational-wave detection searches and parameter estimation efforts would benefit from using SEOBNRv2 waveform templates when focused on neutron star - black hole systems with  $q \lesssim 7$  and  $\chi_{\text{BH}} \approx [-0.9, +0.6]$ . For larger black hole spins and/or binary mass-ratios, we recommend the models be further investigated as NR simulations in that region of the parameter space become available.

## I. INTRODUCTION

The Advanced Laser Interferometer Gravitational-wave Observatory (aLIGO) [1, 2] is currently being commissioned and will begin observation in 2015, reaching its design sensitivity by 2018 – 19. The Virgo gravitational-wave observatory [3] will begin operation in 2016. With improved sensitivity, these detectors will access a thousand times as much volume as their first generation counterparts. In addition, the KAGRA detector is currently under construction in Japan [4], and a plan to build an advanced LIGO detector in India is under consideration. Compact binaries are the most promising sources of gravitational waves (GWs) for aLIGO. Binary systems containing stellar-mass black holes (BH) and/or neutron stars (NS) inspiral and merge because of their GW emission. The GW waves emitted with frequencies above  $\sim 10$  Hz will be in the sensitive band of aLIGO and Virgo.

In this paper, we focus on neutron star – black hole (NSBH) binaries. Based on our current understanding of the astrophysical NS and BH population, stellar binary evolution, and on population synthesis studies, we expect aLIGO to observe 0.2 – 300 NSBH binary mergers a year [5]. GW observations of NSBH binaries have significant scientific potential, beyond

the initial discovery of a new class of astrophysical systems. GWs emitted by coalescing NSBH binaries carry signatures of strong-field gravitational dynamics. Unlike binary neutron stars, GWs from NSBH binaries will contain the signatures of the interaction of BH spins [6–11] with the orbital motion. Significant efforts are underway to access this information using the aLIGO and Virgo detector network to test general relativity in the strong gravity regime [12, 13]. The observation and characterization of a population of NSBH sources will also shed light on stellar evolution and compact-binary formation mechanisms: e.g., a gap in the mass distribution of NSs and BHs could shed light on the mechanism of supernova explosions [14–16]. An unambiguous detection of GWs from a NSBH system accompanied by electromagnetic observations could provide information about the internal structure of NSs [17] and could provide strong evidence linking compact binary mergers and short Gamma-ray bursts (SGRBs) [18–21]. However, unlocking the full scientific potential of GWs emitted by NSBH coalescences requires both detecting as many of such signals as possible and accurately characterizing them to understand the properties of their source binaries.

Detection searches are based on the matched-filtering technique [22], using modeled waveforms as filter templates. Searches for compact binaries with initial LIGO and Virgo detectors used non-spinning template waveforms [23–27] (with

\* prayush.kumar@ligo.org

the exception of [28], ChrisVDBrock et al). While the cataloged astrophysical population of NSs have small spins (mass-normalized  $|\chi| \lesssim 0.05$ ), the spins of stellar-mass BHs are uncertain, with estimates ranging from low to nearly extremal values (i.e., nearly as fast as possible—see, e.g. [11, 29, 30] for examples of nearly extremal estimates of BH spins, and see Refs. [31, 32] for recent reviews of astrophysical BH spin measurements). Recent work has shown that including non-precessing (that is, aligned) component spins in templates used in matched-filtering gravitational-wave searches will significantly improve the searches’ sensitivity [33]. Therefore, aLIGO-Virgo searches targeting NSBH binaries plan to use aligned-spin waveform templates [34]. Because they are central to matched-filtering searches, it is crucial to have GW models that accurately capture the NSBH coalescence process. Modeling inaccuracy would reduce the signal-to-noise ratio (SNR) recovered by detection searches, and degrade the range of aLIGO-Virgo observatories. It would also lead to systematic, but not necessarily controlled, biases in the recovered masses and spins of the source.

Studies of the accuracy of contemporary waveform models in the past have focused on post-Newtonian (PN) [35] and recent Effective-One-Body (in particular, the “SEOB-NRv1” [36]) models. It has been shown that PN approximants disagree significantly with each other and with SEOB-NRv1 for aligned-spin NSBH binaries [37], despite the inclusion of the highest-known order spin contributions to the binary phasing [38, 39]. While the accuracy of the SEOBNR models is enhanced through calibration against high-accuracy Numerical Relativity (NR) merger simulations, most of these simulations correspond to comparable mass ratios. Therefore, the extension of SEOBNR into NSBH parameter space is not guaranteed to be reliable.

In this paper, we systematically investigate waveform approximants in the context of NSBH binaries. Unlike past studies, we investigate not just the *precision* (mutual agreement of approximants) but also their *accuracy*, by comparing with long NR simulations with  $q = m_{\text{BH}}/m_{\text{NS}} = \{5, 7\}$  and aligned BH spin  $\chi_{\text{BH}} = S_{\text{BH}}/M_{\text{BH}}^2 = \{\pm 0.4, \pm 0.6, -0.9\}$ . (Note that, except where we specify otherwise, we adopt geometrized units with  $G = c = 1$  in this paper). These simulations are described further in Sec. II. In addition to PN and SEOBNRv1, we compare with the more recent SEOBNRv2 and the phenomenological PhenomC [40] models. We use the zero-detuning high power noise curve for Advanced LIGO [41] with a 15 Hz lower frequency cutoff in our calculations. We allow the BH spin to vary over  $[-1, 1]$ , and its mass to vary over  $[3M_{\odot}, 14M_{\odot}]$ . The NS mass is fixed at  $m_{\text{NS}} = 1.4M_{\odot}$  with  $\chi_{\text{NS}} = 0$ , as is consistent with the observed astrophysical NS population [42–44]. Note that while investigating waveform modeling errors, we ignore NS matter effects and treat the NS as a low-mass BH. Although matter effects are expected to be measurable by aLIGO (e.g. [45, 46]), they affect the inspiral phasing starting at 5PN order. As there are lower-order spin-dependent vacuum terms in PN phasing that remain unknown, the effect of ignoring matter-dependent secular terms will be sub-dominant to other sources of error in waveform models. We also ignore the effect of NS disruption

before merger, which is likely when the mass-ratio  $m_{\text{BH}}/m_{\text{NS}}$  is small and/or the BH has relatively high aligned spin [47]. However, this disruption occurs at fairly high frequencies, i.e. at  $f_{\text{GW}} \gtrsim 1.2$  kHz [47], and its effects are expected to be small due to the significantly reduced sensitivity of aLIGO at such frequencies [48]. We leave the study of this effect to future work.

First, we study GW model *precision* by comparing the PN time-domain TaylorT4, PN frequency-domain TaylorF2, SEOBNRv1 and PhenomC models with the most recent SEOBNRv2 model. As SEOBNRv2 has been calibrated to 38 NR simulations, we take it as the fiducial model representing the true waveform. We find that both PN models have overlaps with SEOBNRv2 *below* 0.9 for mass-ratio  $q \geq 3$  and/or BH spin  $|\chi_{\text{BH}}| \geq 0.5$ . We also find that PhenomC and SEOBNRv2 have overlaps below 0.9 for  $q \leq 5$  and/or BH spin  $|\chi_{\text{BH}}| \geq 0.3$ , falling as low as 0.6. Finally, we also find the overlaps between SEOBNRv1 and SEOBNRv2 fall below 0.9 for NSBH systems with anti-aligned BH spins  $\chi_{\text{BH}} \leq -0.5$ .

We further investigate the *accumulation of mismatch* between different models, as a function of GW frequency. For PN approximants, we find that most of the mismatch is accrued during the late-inspiral phase when the PN velocity parameter  $v/c \gtrsim 0.2$ . This is expected, because PN results are perturbative expansions in  $v/c$  that break down when  $v$  becomes comparable to  $c$  near the time of coalescence. Between SEOBNRv1 and SEOBNRv2, we find that mismatch is accrued during the early-to-late inspiral transition period when  $v/c \lesssim 0.26$ . We find a similar trend between PhenomC and SEOBNRv2. This demonstrates discrepancies between NR-calibrated models in the early inspiral phase, despite good agreement close to merger, where all of the models have been calibrated to NR.

Second, we study the *accuracy* of NSBH waveform models by computing their overlaps (or *faithfulness*) against our long NR simulations. Our simulations extend down to  $v/c \simeq 0.2$ , and are long enough to probe the frequency range in which SEOBNRv1/PhenomC phase evolutions differ from SEOBNRv2. We find that SEOBNRv1 has 1 – 3% mismatches against the aligned-spin simulations, which rise up to  $\sim 5\%$  against the anti-aligned-spin ones. While most of this mismatch is accumulated during the last few pre-merger orbits for *aligned*-spin cases, for *anti-aligned* cases it accumulates over the 30 – 50 inspiral orbits that our simulations span. On the other hand, we found that SEOBNRv2 has  $< 1\%$  mismatches with NR, for both aligned and anti-aligned simulations. Therefore, we conclude that the differences between the two SEOBNR models are because of the phasing errors in SEOBNRv1. For PhenomC and both PN approximants, we find  $\geq 10\%$  mismatches against NR, for both aligned and anti-aligned spin simulations. We therefore conclude that SEOBNRv2 provides the most accurate description of aligned-spin NS-BH coalescence waveforms, with the caveat that the model should be analyzed for more extreme component spins.

Third, we investigate the *suitability of different models for detection searches*. To address this question, we compute the *effectualness* of different models by allowing the addi-

tional degree of freedom of maximizing overlaps between analytic and numerical waveforms over intrinsic binary parameters. We find that both SEOBNRv1 and SEOBNRv2 recover  $\geq 99.8\%$  of the optimal SNR. PhenomC shows low SNR recovery, which drops below  $\sim 90\%$  for anti-aligned BH spins. We therefore recommend against using this model in NSBH detection searches. Both PN models recover about 98% of the SNR for aligned-spin systems, and are therefore effectual for aLIGO searches. For anti-aligned systems, both TaylorT4 and TaylorF2 models recover  $\lesssim 96\%$  of the SNR and would likely benefit from the computation of higher order spin-dependent corrections to PN dynamics. Therefore we recommend that SEOBNRv2 be preferred in aLIGO NSBH detection searches.

Finally, we probe the question of *systematic biases in parameter recovery* corresponding to using each approximant to model aLIGO parameter estimation templates. We find that the accuracy of the chirp mass ( $\mathcal{M}_c = (m_1 m_2)^{3/5} (m_1 + m_2)^{-1/5}$ ) recovery increases with the number of orbits that are integrated over. All approximants recovered  $\mathcal{M}_c$  within a few percent. The spin-mass-ratio degeneracy makes the accurate determination of mass-ratio and component spins more challenging. We find systematic biases in mass-ratio to be between a few to tens of percents, increasing with BH spin, with similar biases in the recovered values of BH spins. Of all the models considered, we find that SEOBNRv2 surpasses others in faithfulness. Using the accuracy measures proposed in [49], we also found SEOBNRv2 to be indistinguishable from true waveforms up to SNRs  $\approx 8 - 14$  ( $16 - 18$ ) for aligned (anti-aligned) BH spins. We therefore recommend that SEOBNRv2 be used in aLIGO parameter estimation efforts for aligned-spin NSBH detection candidates, but we also recommend that SEOBNR be tested for higher component spins.

Our results are limited by the fact that our NR waveforms only extend down to  $v/c \simeq 0.21 - 0.24$  (i.e.  $60 - 80$  Hz for NSBH masses), while aLIGO is sensitive down to 15 Hz. A sizable fraction (35 – 45%, depending on BH spin) of the signal power will be accumulated at frequencies below this range. We plan to extend these calculations to lower frequencies in future work.

The remainder of the paper is organized as follows: In Sec. II, we describe the NR waveforms presented in this paper and discuss their convergence. In Sec. III, we describe the waveform models studied here. In Sec. IV, we describe the measures used to quantify waveform discrepancies. In Sec. V, we discuss the faithfulness of different waveform approximants for different NSBH masses and spins, and also as a function of the emitted GW frequency. In Sec. VI, we investigate the late-inspiral accuracy of all approximants using our high accuracy numerical simulations. In Sec. VII, we study the viability of using different approximants as detection templates, as well as their intrinsic parameter biases for aLIGO parameter estimation studies. In Sec. VIII, we summarize and discuss our results.

## II. NUMERICAL RELATIVITY SIMULATIONS

We construct our NR waveforms using the Spectral Einstein Code (SpEC) [50]. Their parameters are summarized in Table I. Of particular note is the length of these simulations; the shortest waveform presented here has over 36 orbits of inspiral before the merger and the longest has nearly 90 orbits. Fig. 1 shows the real part of the waveform dimensionless strain,  $rh_{22}/M$  for each of the simulations on Table I. With the exception of the 176 orbit simulation presented in [51] and a 48.5 orbit simulation presented in [52] these waveforms are among the longest done to date. The longest waveform currently in the SXS catalog is only 35.5 orbits [53].

To test the accuracy of the simulations we ran each simulation using different numerical resolutions; we label each resolution by an integer  $N$ , where larger  $N$  indicates finer resolution. We compute the phase of the  $\ell = 2, m = 2$  mode of  $\Psi_4$  (the second time derivative of the complex strain  $h_{22}(t)$ ) for different resolutions Fig. 2 shows these phase differences for each pair of resolutions for five of the seven numerical simulations presented here. (We ran the other two simulations at fewer than 3 values of  $N$ , so such a plot would not be useful for those cases.)

If for all subdomains, i) the number of grid points increased uniformly with increasing  $N$ , and ii) at any given time, the locations of the boundaries of all subdomains were independent of  $N$ , then Fig. 2 would represent a classic convergence test. In that case, the phase differences should decrease with  $N$  in a predictable way, according to the convergence order of the numerical scheme. The simulations here, however, use a spectral adaptive mesh refinement (AMR) scheme [54], and the label  $N$  determines the error tolerance used by AMR when it decides whether to change the number of points in a given subdomain and when it decides whether to split a single subdomain into many smaller ones or to join several subdomains into a larger one. Because AMR makes these decisions independently for different values of  $N$ , at any given time it is possible that a given subdomain has the same number of grid points for two values of  $N$ , and it is possible that subdomain boundaries for different values of  $N$  do not agree. Therefore, we do not necessarily expect strict convergence in Fig. 2. These issues will be discussed in detail in a separate paper that focuses on convergence of BBH runs using SpEC.

Nevertheless, for the  $\chi = \pm 0.6$  simulations, the differences converge well with  $N$ : differences become successively smaller with increasing resolution. Furthermore, the difference between  $N = 3$  and  $N = 2$  is approximately equal to the difference between  $N = 4$  and  $N = 2$ , indicating that these differences essentially measure the error in  $N = 2$ . For the  $\chi = \pm 0.4$  and  $\chi = -0.9$  simulations, the difference between  $N = 3$  and  $N = 2$  is smaller than the difference between  $N = 3$  and  $N = 1$ , but the spacing between differences is not uniform, and there are some anomalously small phase differences, such as between  $N = 2$  and  $N = 1$  for  $\chi = 0.4$ .

For  $\chi = \pm 0.6$ , the difference between the two finest resolutions  $N = 3$  and  $N = 4$  is a good measure of the numerical error in the  $N = 3$  simulation. The error in  $N = 4$  could be similarly measured via the difference between  $N = 4$  and  $N = 5$ ,

ID	$q$	$\vec{\chi}_1$	No. of orbits	Initial $f_{gw}$ (Hz)	Initial $M\omega_{orbital}$	$\dot{a}$	$D_0$	$\epsilon$
SXS:BBH:0202	7	(0, 0, 0.6)	62.1	75.5	0.01309	$4.3970 \times 10^{-5}$	17.0000	$9 \times 10^{-5}$
SXS:BBH:0203	7	(0, 0, 0.4)	58.5	76.0	0.01317	$-9.8403 \times 10^{-6}$	17.0005	$< 1.6 \times 10^{-4}$
SXS:BBH:0204	7	(0, 0, 0.4)	88.4	60.3	0.01045	$-4.6373 \times 10^{-6}$	20.0000	$< 1.7 \times 10^{-4}$
SXS:BBH:0205	7	(0, 0, -0.4)	44.9	76.0	0.01318	$-1.4760 \times 10^{-5}$	17.1036	$7.0 \times 10^{-5}$
SXS:BBH:0206	7	(0, 0, -0.4)	73.2	59.8	0.01036	$-7.8300 \times 10^{-6}$	20.2167	$< 1.6 \times 10^{-4}$
SXS:BBH:0207	7	(0, 0, -0.6)	36.1	80.8	0.01399	$7.1708 \times 10^{-6}$	16.4000	$1.693 \times 10^{-4}$
SXS:BBH:0208	5	(0, 0, -0.9)	49.9	80.0	0.0104	$-4.5088 \times 10^{-5}$	20.0778	$5.074 \times 10^{-4}$

TABLE I. Numerical-relativity simulations used in this study (each performed using SpEC [50]). For each simulation (labeled by ID), the table shows the mass ratio  $q \equiv m_1/m_2 \geq 1$ , the spin  $\vec{\chi}_1$  of the heavier compact object (the lighter object is non-spinning), the number of orbits, the initial gravitational-wave frequency  $f_{gw}$  when the total mass is scaled so that the system mimics a NSBH binary with a NS mass of  $1.4M_\odot$ , the initial dimensionless orbital velocity  $M\omega_{orbital}$ , radial velocity  $\dot{a}$ , separation  $D_0$ , and eccentricity  $\epsilon$ . These values listed for  $f_{gw}$ ,  $M\omega_{orbital}$ ,  $\dot{a}$  and  $D_0$  are for the initial data, before junk radiation. The  $\vec{\chi}_1 = \pm 0.4$  simulations use CFMS initial data while the rest use SKS initial data.

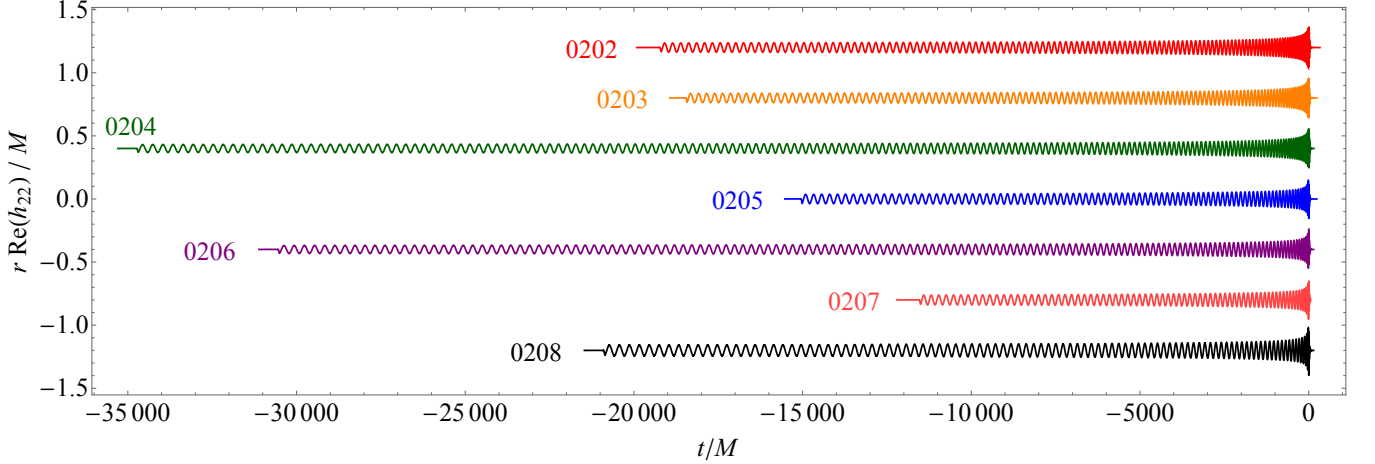


FIG. 1. The real part of  $rh_{22}/M$  of the  $\ell = m = 2$  mode of the numerical waveforms used in this paper, where  $M$  is the total mass and  $r$  is the radial distance from the source to an observer. The waveform labeled by  $N$  correspond to simulation SXS:BBH: $N$ , where  $N \in \{202, 203, 204, 205, 206, 207\}$ . The waves are shown as a function of time  $t$ . A constant vertical offset is applied to each waveform for clarity, and the waves are offset in time so the peak amplitude occurs at time  $t = 0$ .

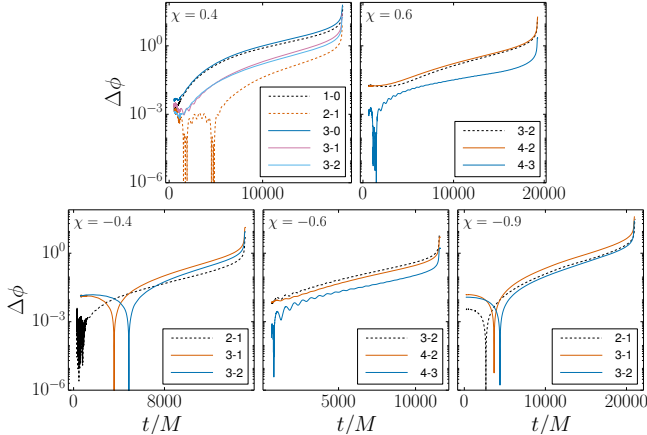


FIG. 2. Phase differences between different resolutions for the  $\ell = 2, m = 2$  modes of  $\Psi_4$ , plotted as a function of time. Only the five numerical simulations with more than 2 resolutions are displayed. The legends indicate which resolutions are compared, e.g. “3-2” compares the phase of  $N = 3$  versus  $N = 2$ .

but since we do not have an  $N = 5$  simulation, we take the difference between  $N = 3$  and  $N = 4$  as an extremely conservative estimate of the error in  $N = 4$ . For  $\chi = \pm 0.4$  and  $\chi = -0.9$ , where the convergence with  $N$  is not so apparent, we likewise take the difference between the two highest resolutions as the error estimate of the highest-resolution simulation; in these cases the error estimate is likely not as conservative as for  $\chi = \pm 0.6$ .

### III. WAVEFORM APPROXIMANTS

In this paper, we consider three waveform families: post-Newtonian, Effective-One-Body, and phenomenological models [40, 55]. We briefly summarize them here, pointing the reader to the references for more detailed descriptions. We consider the  $(\ell, m) = (2, \pm 2)$  spin-weighted spherical harmonic waveform multipoles, since (i) these are the dominant modes for non-precessing systems, with the contributions from other modes being smaller by a few orders of magnitude, and (ii) none of the contemporary IMR models include



the sub-dominant waveform modes.

**Post-Newtonian:** The Post-Newtonian (PN) approximation is a perturbative expansion of compact binary inspiral dynamics in the limit of slow motions and weak fields. The orbital energy  $E$  of a non-precessing binary and the flux  $F$  of the gravitational energy emitted as GWs are known to 3.5PN order [56–64]. Combining  $E$  and  $F$  using the energy balance equation  $dE/dt = -F$  yields a system of differential equations; solving these equations gives the GW phase and the orbital frequency evolution. The energy balance equation can be re-expanded and solved in different ways to obtain different approximants that agree to 3.5PN order but differ at higher orders. The PN formalism and the corresponding equations of motion break down before merger as the underlying approximations (slow motions and weak fields) break down; therefore, the PN formalism produces only the inspiral portions of the waveform. In this paper, we will examine two particular PN approximants, the time-domain TaylorT4 and frequency-domain TaylorF2. In both, we include the recently published spin-orbit tail (3PN) and the next-to-next-to-leading order spin-orbit (3.5PN) contributions [65, 66]. We refer the reader to the Appendix of Ref. [37] for a summary of the expressions that describe both approximants.

**Effective-One-Body:** The Effective-One-Body (EOB) approach solves for the dynamics of a compact binary system by mapping them to the dynamics of an effective test particle of mass  $\mu = m_1 m_2 / (m_1 + m_2)$  with a spin  $S^*(m_1, m_2, S_1, S_2)$  in a space-time described by a suitable deformation of the Kerr metric. Specifically, when constructing model waveforms using the EOB approach, one chooses the deformation and the test-particle spin such that the geodesic followed by the test particle reproduces the PN-expanded dynamics of the compact binary system with component masses  $m_1$  and  $m_2$  and spins  $S_1$  and  $S_2$ . Then, one matches the coefficients of the deformed metric to the PN expansion up to 3PN order; to further improve accuracy, one adds adjustable 4PN and 5PN terms that are calibrated by forcing agreement with NR waveforms. The conservative dynamics of the test particle in the deformed-Kerr spacetime are described by the EOB Hamiltonian  $H_{\text{EOB}}$ . The expressions for  $H_{\text{EOB}}$  for different Spinning-EOB (SEOBNR) models differ at high PN orders and can be found in Refs. [36, 67]. Further, a radiation reaction term in the equations of motion captures the non-conservative dynamics, i.e., the motion of the binary through inspiral to merger [36, 67]. In contrast to PN waveforms, EOB waveforms continue through merger and ringdown, with the ringdown waveform constructed as a linear superposition of the first eight quasi-normal modes (QNMs) of the Kerr BH formed at binary merger [68]. Matching the ringdown waveform to the inspiral-merger portion determines the coefficients associated with these QNMs.

We use two SEOBNR models (both available in the LIGO Algorithm Library (LAL) [69]) in this study: SEOBNRv1 and SEOBNRv2. These models differ in their calibration to NR waveforms. SEOBNRv1 models the inspiral-merger-ringdown (IMR) waveform for binaries with component spins  $-1 \leq \chi_{1,2} \leq 0.6$ ; while SEOBNRv2 can model more extremal component spins, i.e.  $-1 \leq \chi \leq 0.99$ . SEOB-

NRv1 uses 5 non-spinning NR simulations at mass ratios  $q = \{1, 2, 3, 4, 6\}$  and two equal-mass simulations with  $\chi_{1,2} = \pm 0.4$  to choose six adjustable parameters; note that NSBH systems are outside the domain of calibration of this model. SEOBNRv2, in addition, includes an adjustable parameter in the effective particle spin mapping, one in the Hamiltonian, and one in the complex phase of  $h_{2,2}$ . These parameters have been calibrated against 8 non-spinning and 30 aligned-spin NR waveforms. We refer the readers to Ref. [36] and Ref. [67] for comprehensive descriptions of SEOBNRv1 and SEOBNRv2, respectively.

**Phenomenological model:** PhenomC is a phenomenological model that has a closed form in the frequency domain and describes the GW emitted by aligned spin binaries during their inspiral-merger-ringdown (IMR) phases [40]. Closed form TaylorF2 expressions capture the early adiabatic inspiral stage of binary coalescence, with the frequency-domain waveform amplitude and phase expressed as expansions in GW frequency. PhenomC inspiral phasing includes non-spinning terms up to 3.5PN order, spin-orbit and spin-spin coupling terms up to 2.5PN order, and horizon absorption terms up to 2.5PN order [70]. In the late-inspiral/pre-merger regime, the PN approximation is insufficient to model the phase evolution accurately; instead, a phenomenologically fitted power series in frequency (i.e., a polynomial in  $f^{1/3}$ ) captures the phase evolution. Calibrating against a set of NR waveforms [40] in the frequency range  $[0.1 f_{\text{RD}}, f_{\text{RD}}]$ , where  $f_{\text{RD}}$  is the primary (least damped) GW frequency emitted during the quasi-normal ringing of the post-merger black hole remnant, determines the free coefficients in the resulting *pre-merger* phase prescription. In the ringdown regime, PhenomC models the phase as a linear function in GW frequency, capturing the effect of the leading quasi-normal mode. Similarly, PhenomC constructs the amplitude prescription through piecewise modeling of the pre-merger and ringdown regimes, approximating the amplitude by a power-series in  $f^{1/3}$  pre-merger and by a Lorentzian post-merger. For a complete description of PhenomC and its calibration, we refer the reader to Ref. [40]. Note that PhenomC belongs to the unique class of models that are both closed-form in the frequency domain, *and* include the late-inspiral, merger, and ringdown in the waveforms. These features are especially convenient for real GW searches, which operate in the frequency domain, filtering observatory data with a large number ( $10^5 - 10^6$ ) of waveform templates.

#### IV. QUANTIFYING WAVEFORM ACCURACY

As a measure of how “close” two waveforms  $h_1$  and  $h_2$  are in the waveform manifold, we use the maximized overlap (match)  $\mathcal{O}$ , defined by

$$\mathcal{O}(h_1, h_2) \equiv \frac{\max_{\phi_c, t_c} (h_1 | h_2(\phi_c, t_c))}{\sqrt{(h_1 | h_1)(h_2 | h_2)}}, \quad (1)$$

where the overlap  $(\cdot|\cdot)$  between two waveforms is

$$(h_1|h_2) \equiv 4 \int_{f_{\min}}^{f_{\text{Ny}}} \frac{\tilde{h}_1(f)\tilde{h}_2^*(f)}{S_n(f)} df; \quad (2)$$

$\phi_c$  and  $t_c$  are the phase and time shift differences between  $h_1$  and  $h_2$ ;  $\tilde{h}(f)$  is the Fourier transform of the GW waveform  $h$ ;  $S_n(f)$  is the one-sided power spectral density (PSD) of the detector noise, which we assume to be stationary and Gaussian with zero mean;  $f_{\min}$  is the lower frequency cutoff for filtering; and  $f_{\text{Ny}}$  is the Nyquist frequency corresponding to the waveform sampling rate. The normalization of  $\mathcal{O}$  takes away the effect of any overall amplitude scaling differences between  $h_1$  and  $h_2$ . The complimentary measure of the *mis-match*  $\mathcal{M}$  between the two waveforms is therefore

$$\mathcal{M}(h_1, h_2) = 1 - \mathcal{O}(h_1, h_2). \quad (3)$$

Matched-filtering based searches use a discrete bank of modeled waveforms as filters. The optimal value of the recovered SNR is  $\rho_{\text{opt}} = \sqrt{(h^{\text{tr}}|h^{\text{tr}})}$ , where  $h^{\text{tr}}$  is the actual GW signal in the detector output data. With a finite bank of filter templates, the recovered SNR is  $\rho \simeq \mathcal{O}(h^{\text{tr}}, h_b) \rho_{\text{opt}} \leq \rho_{\text{opt}}$ , where  $h_b$  is the filter template in the bank that has the highest maximized overlap with the signal  $h^{\text{tr}}$ ; i.e. the recovered SNR is maximized over both intrinsic (component mass and spin) and extrinsic ( $\phi_c$  and  $t_c$ ) parameters that describe the source binary. For a NSBH population uniformly distributed in spatial volume, the detection rate is  $\propto \mathcal{O}(h^{\text{tr}}, h_b)^3$ . To maximize the detection rate, it is therefore crucial for the model waveform manifold, containing  $h_b$ , to faithfully reproduce the manifold of true waveforms that contains  $h^{\text{tr}}$ .

In this paper, we take  $S_n(|f|)$  to be the *zero-detuning high power* noise curve for aLIGO [41, 48]. The peak GW frequency for the lowest binary masses that we consider, i.e. for  $m_1 + m_2 \simeq 8.4M_\odot$ , is  $\sim 3$  kHz during ringdown. We sample the waveforms at 8192 Hz, preserving the information content up to the Nyquist frequency  $f_{\text{Ny}} = 4096$  Hz.

Our numerical waveforms begin at relatively low frequencies (between about 60 Hz and 80 Hz), but nevertheless they do not completely span the detector's sensitive frequency band. The discontinuity at the start of the NR waveform, because of Gibbs phenomena [71], corrupts the Fourier transform. We therefore taper the start of the waveforms using a cosine tapering window, whose width is chosen to control the corruption of the resulting waveform in a way that the mismatches because of tapering stay below 0.2%. Additionally, to minimize residual spectral leakage, we apply an eighth order Butterworth high-pass filter with the cutoff frequency equal to the frequency of the waveform at the end of the tapering window. In Sec. VIB, we measure the effect of waveform conditioning on the NR waveforms by comparing identically conditioned waveforms against unconditioned-but-significantly-longer SEOBNRv2 waveforms.

## V. COMPARISON OF WAVEFORM MODELS

In this section, we show the faithfulness between waveforms from different approximants, where we choose the

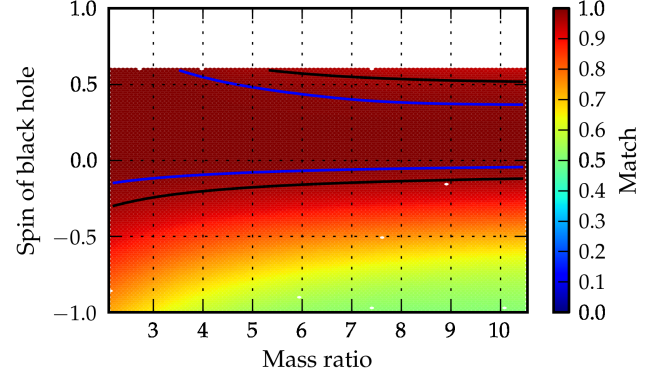


FIG. 3. In this figure, we show the match between the two SEOBNR models we consider in this paper, as a function of the BH spin and binary mass ratio. The mass of the NS is fixed at  $1.4M_\odot$ , and its spin is set to 0, consistent with the observed astrophysical population of NSs [42]. The blue (black) solid lines are the contours of 99% (97%) match. We find that the matches between the models drop sharply for  $\chi_{\text{BH}} \leq -0.15$ .

physical parameters to be consistent with NSBH sources. We compare the inspiral-merger-ringdown (IMR) models SEOBNRv1 and PhenomC, and the PN models TaylorT4 and TaylorF2, with the SEOBNRv2 model. We also show how the disagreement between approximants builds up over the course of a binary's inspiral, by computing their faithfulness over different GW frequency intervals. For both, we take SEOBNRv2 as the fiducial model because it has been calibrated against the highest number of high-accuracy NR simulations of aligned-spin binaries (38 in total, with mass ratio up to  $\sim 8$ ), and is therefore likely to be the most accurate representation of true waveforms available at present). Overall, we find that (i) the two SEOBNR models (SEOBNRv1,2) disagree significantly for anti-aligned spinning binaries (matches below 80%), with their mismatches accumulating over lower frequency inspiral orbits; (ii) PhenomC and SEOBNRv2 produce drastically different waveforms over most of the NSBH parameter space, except for the small mass-ratio + small spin corner; and (iii) both PN models show slightly better agreement with SEOBNRv2 than PhenomC, but still restricted to small mass-ratios and small component spins, which is consistent with [37].

### A. Faithfulness of models

In Fig. 3, we examine the faithfulness of the two SEOBNR models. Neither of these models were used as templates in past LIGO searches, because they were published after initial LIGO searches were completed, but both are promising candidate models for aLIGO. Focusing on stellar-mass NSBH binaries, we fix the NS mass to  $1.4M_\odot$ , the NS spin to 0, and allow the BH mass to vary over  $[3, 15]M_\odot$  and the BH spin to vary over the allowed range of SEOBNRv1  $[-1, 0.6]$  [36]. We see that the agreement between the models is primarily influenced by the BH spin and secondarily by the mass ra-

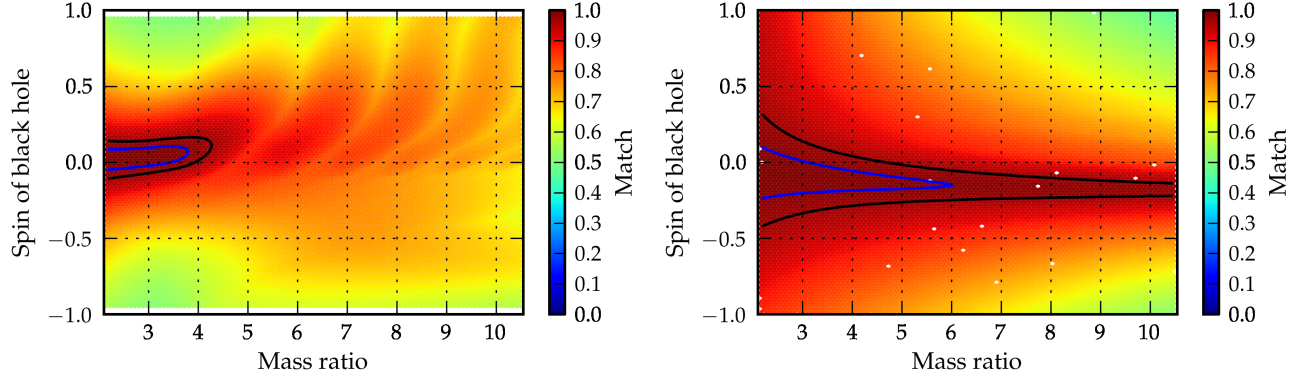


FIG. 4. These plots are similar to Fig. 3, except they compare SEOBv2 with PhenomC (left panel) and TaylorF2 (right panel). From the left panel, we observe that PhenomC and SEOBv2 are faithful to each other for very small BH spins and  $q = m_1/m_2 \lesssim 4$ . Their matches drop sharply for moderately spinning binaries and also above moderate mass-ratios. Also, the fall in matches of PhenomC with increasing mass-ratio is not monotonic. In the right panel, we find good agreement between TaylorF2 and SEOBv2 for binaries with very small BH spin. The best agreement, however, is for small anti-aligned spins, with the two models having  $\lesssim 95\%$  matches for non-spinning binaries. Note that PhenomC uses TaylorF2 phasing prescription the early inspiral, including, however, only the leading and next-to-leading order spin-dependent terms.

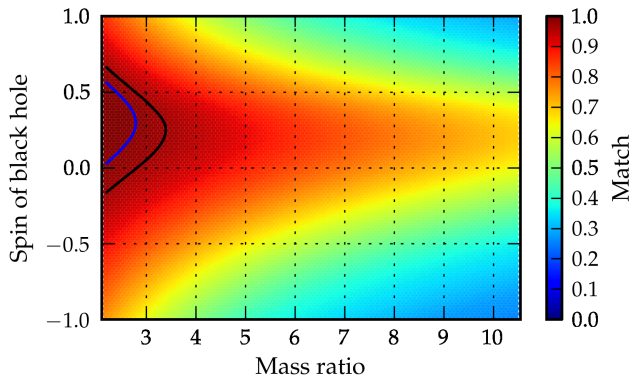


FIG. 5. This figure is similar to Fig. 3, except it compares TaylorT4 with SEOBv2. We find that for mass ratios  $q \geq 3.5$  or BH spin  $\chi_{\text{BH}} \notin [-0.1, 0.6]$ , the two models disagree significantly, with matches falling below 0.9, down to 0.4.

tio. As expected, both agree in the comparable mass and non-spinning limits, where both incorporate information from NR simulations. We also find good agreement for *aligned* BH spins. However, when the BH spin is *anti-aligned* with the orbital angular momentum, SEOBv1 and SEOBv2 produce *significantly* different waveforms, with matches dropping below 0.8 for  $\chi_{\text{BH}} \leq -0.5$ . This demonstrates that the more recent SEOBv2 model incorporates different spin-dependent phasing terms. However, to make statements about the *accuracies* of either, we must analyze both using high-accuracy NR waveforms, a comparison we turn to in the next section.

In Fig. 4, we show the faithfulness of the PhenomC (left panel) and TaylorF2 (right panel) models against SEOBv2. We notice that PhenomC agrees with SEOBv2 *only* for very mildly spinning binaries with  $|\chi_{\text{BH}}| \lesssim 0.1$  and compa-

rable mass ratios  $q \lesssim 4$ . Over the remainder of the parameter space, the matches between PhenomC and SEOBv2 were found to be low. This is somewhat surprising, since PhenomC has been calibrated against spinning NR simulations with  $q$  up to 4 as well, albeit spanning fewer orbits and produced using a different NR code [72, 73]. Comparing with the right panel of Fig. 4, we find that TaylorF2 agrees with SEOBv2 more closely for rapidly spinning NSBH systems with  $q \lesssim 3$ , as well as for binaries with small BH spin magnitude at all mass ratios. Since the inspiral portion of PhenomC phasing is the same as TaylorF2 (with the caveat that the former does not include the recently published spin-dependent 3 PN and 3.5 PN contributions [65, 66]), we conclude that their differences arise from the post-merger phasing prescription of PhenomC. We study this further later in this section, where we highlight the phase of binary coalescence where different approximants disagree.

We further show the faithfulness between TaylorT4 and SEOBv2 models in Fig. 5. We find that their faithfulness drops sharply with increasing mass ratio, falling below 0.9 for mass-ratios  $q \gtrsim 4$  for all values of BH spin. *Only* for near-equal mass low-spin binaries does TaylorT4 agree well with SEOBv2, which is consistent with past comparisons with NR simulations (e.g., Fig. 7 of [74]). Comparing with the right panel of Fig. 4, we see that (a) TaylorF2 has better overall agreement with SEOBv2, and (b) TaylorF2 agrees better for small anti-aligned spins and TaylorT4 for small aligned spins. These differences are expected to decrease in future PN approximants, as higher order PN terms become available.

## B. Accumulation of mismatches with frequency

For the adiabatic early-inspiral phase where the binary is well separated and inspirals relatively slowly, all GW models



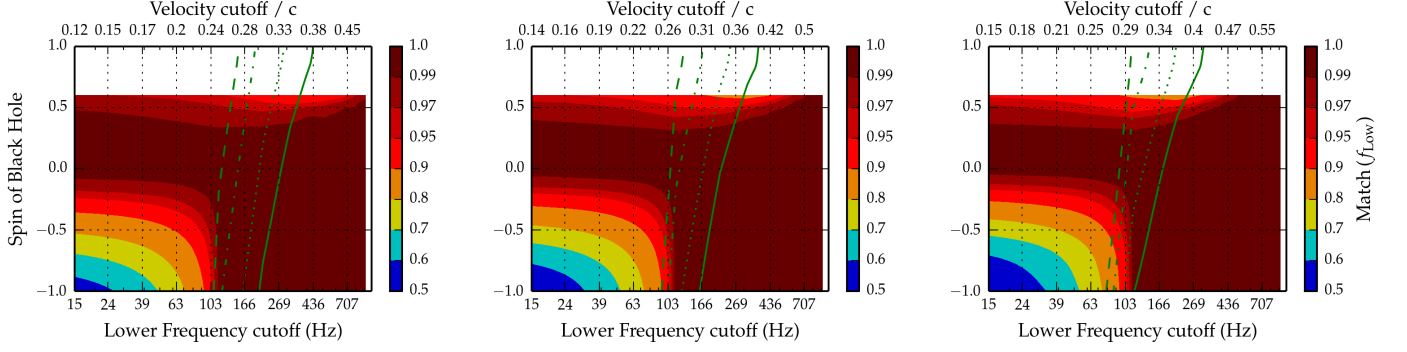


FIG. 6. In this figure, we show the accumulation of mismatch between the two SEOBNR models that we consider in this paper by plotting the match (shown by colors) as a function of the low-frequency cutoff in the match calculation (horizontal axes) and black-hole spins (vertical axes). We choose 3 sets of NSBH systems corresponding to  $q = \{5, 7, 10\}$  and  $m_{\text{BH}} = \{7M_{\odot}, 9.8M_{\odot}, 14M_{\odot}\}$  (from left to right panels, respectively). We vary the black-hole spin (vertical axes) over the validity range for SEOBNRv1 [36],  $\chi_{\text{BH}} \in [-1, 0.6]$ . We fix the mass of the neutron star to  $1.4M_{\odot}$  and the spin of the neutron star to zero. The solid, dotted, dash-dotted and dashed lines are contours of the frequencies starting from which the binary merges after 5, 10, 20, 30 orbits, respectively. For anti-aligned BH spins, the matches are high when we integrate over the last few tens of orbits, but they fall *significantly* as we include more orbits (lower frequencies) in the computation. For moderate aligned BH spins, we find dephasing in the late-inspiral which is compensated for by lower frequency orbits. For comparison, the longest Numerical Relativity simulation to which either of the two models considered here have been calibrated to spans about 33 orbits [53, 67].

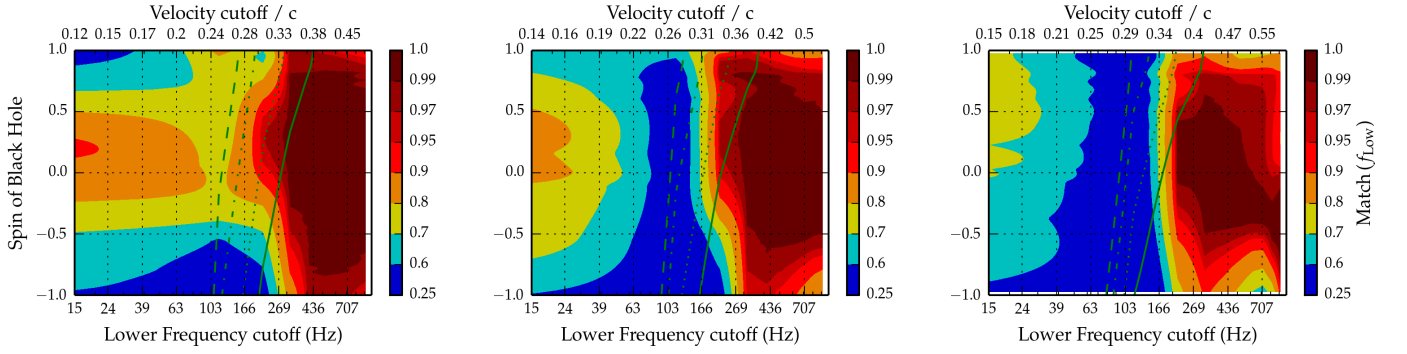


FIG. 7. These figures are similar to Fig. 6, with the only difference that we compare here the PhenomC and SEOBNRv2 models. We observe that the two models agree over the last few ( $< 10$ ) orbits, but their matches drop sharply over earlier late-inspiral orbits. The inclusion of very low-frequency orbits in match calculations leads to an increase in matches for  $|\chi_{\text{BH}}| \leq 0.2$ . The pattern shown in these figures suggests that dephasing is accrued rapidly close to the point where the model switches from TaylorF2 to its pre-merger phasing prescription.

considered here are based on PN results. As the binary tightens, the PN approximation becomes less accurate. In order to capture the late-inspiral/plunge and merger phases, the IMR models either use purely phenomenological prescriptions or re-sum truncated PN results to add terms at all unknown higher orders in a controlled way. In both approaches, the model is calibrated against NR simulations of binary mergers, and models which are more extensively calibrated tend to be more robust. But do the different models agree in the late-inspiral regime, where the PN approximation is not valid and where we have no NR simulations available? To answer this question, we study here the mutual disagreement between models over different phases of binary coalescence.

First, we examine the mismatch accumulation between the two EOB models for three representative sets of NSBH masses. In Fig. 6, the three panels correspond to mass-ratios

$q = m_1/m_2 = \{5, 7, 10\}$  (left to right), with the NS mass fixed at  $1.4M_{\odot}$ . The color shows the match between SEOBNRv1 and SEOBNRv2 as a function of the lower frequency cutoff on the match integral (shown on the x axes), for different values of BH spin (shown on the y axes). The four green curves on each panel are contours of the frequencies that mark “N orbits to merger”, with  $N = 30, 20, 10, 5$ , respectively from left to right. We first note that the two models agree well for non-spinning binaries. When the BH spin is aligned to the orbital momentum, we observe some dephasing for binaries with  $\chi_{\text{BH}} \gtrsim 0.3$ , that accumulates over the last 30 or so orbits. When integrated over the entire waveform, this dephasing gets compensated for by the lower frequency orbits. For anti-aligned BH spins, however, the agreement between the two models is *significantly* low during the early inspiral. Over the last 15 – 20 orbits the two models have matches  $> 0.99$ , but



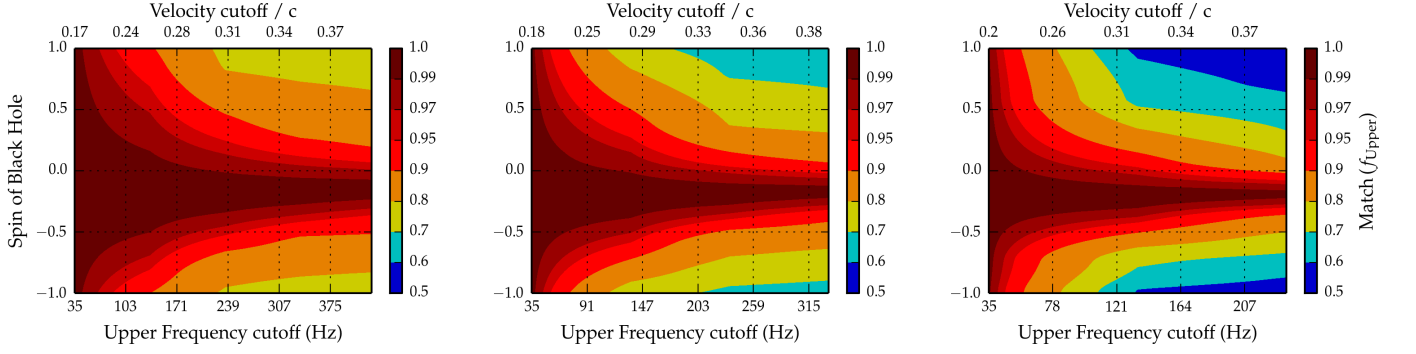


FIG. 8. These figures are similar to Fig. 6 with two differences: (a) here we compare the TaylorF2 and SEOBNRv2 models, and (b) the quantity shown is the match between the models as a function of the upper-frequency cutoff, with the low-frequency cutoff fixed at 15 Hz. Similar to the trend observed in Ref. [37] for SEOBNRv1, TaylorF2 agrees with the SEOBNRv2 model at low frequencies, but their agreement drops *significantly* during and after late-inspiral. The matches drop starting at lower frequencies with increasing BH spin magnitudes. These patterns are consistent with the fact that PN results decrease in accuracy with increasing orbital frequencies, especially as component spins becomes large.

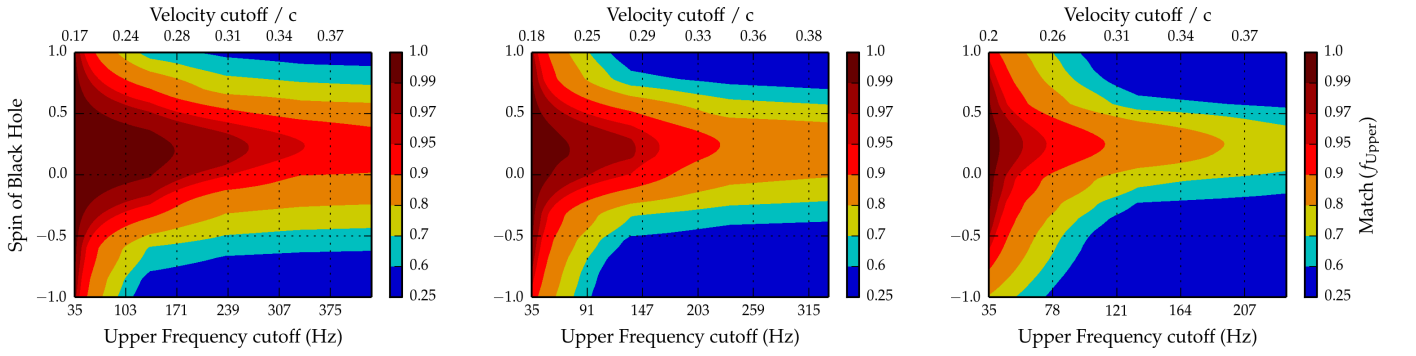


FIG. 9. These figures are similar to Fig. 8 with the only difference that here we compare the TaylorT4 and SEOBNRv2 model. Comparing to Fig. 8, we find that (a) the patterns of mismatch accumulation in these figures are qualitatively similar to TaylorF2, and (b) the disagreement between TaylorT4 and SEOBNRv2 accumulates starting at *lower* frequencies and *more drastically* compared to TaylorF2. These results suggest that higher order PN terms in orbital phasing, especially spin dependent terms, are required to obtain a more accurate PN description of the late-inspiral phase.

they drop below 0.95 around the 20 – 30 orbit mark, and further decrease *monotonically* as lower frequencies are included in the match calculation. Therefore, for anti-aligned spins, we would expect that NR simulations with lengths  $\lesssim 30$  orbits, as used by Ref. [67] for SEOBNRv2, would match well with both the SEOBNRv1 and SEOBNRv2 models, but that they would drastically disagree with at least one of the models early on. Given the lack of clear convergence of the SEOBNR models, we will investigate their *accuracy* in the following section by comparing them to long NR waveforms that probe the low-frequency regime where the models disagree.

Next, we compare the PhenomC and SEOBNRv2 models by computing their matches with varying lower frequency cutoffs. The results are shown in Fig. 7, where all three panels are similar to Fig. 6 with the only difference that SEOBNRv1 is replaced by PhenomC. We first note that the two models agree during the very early inspiral where PhenomC reduces to TaylorF2, as well as over the last few pre-merger orbits.

Most of their dephasing accumulates in a relatively narrow frequency range centered at  $\sim 100$  Hz, which is where PhenomC switches to its phenomenological phasing prescription. We also find that the spin on the BH affects the model agreement in two ways: (i) their dephasing increases with spin magnitude, and (ii) it also increases as the BH spin gets increasingly anti-aligned with the orbital angular momentum.

Inspirational-only PN models have been shown to agree with SEOBNRv1 during early inspiral and to monotonically diverge as the orbital frequency rises [37]. To quantify their agreement with our fiducial model, SEOBNRv2, we compute matches between PN and SEOBNRv2 as a function of the *upper* frequency cutoff (with the lower cutoff fixed at 15 Hz). In Fig. 8 we show the results for TaylorF2, with the upper frequency cutoff on the x-axes, BH spin on the y-axes and colors showing matches. The three panels correspond to the same representative NSBH systems as in Fig. 6. We find that for mildly anti-aligned BH spins with  $\chi_{\text{BH}} \gtrsim -0.2$ , Tay-

lorF2 agrees with SEOBNRv2 through most of late-inspiral. For other BH spin values, the two models start disagreeing at relatively low frequencies, e.g., for a  $q = 5$  binary with  $\chi_{\text{BH}} = -0.6$ , the match drops to 0.9 between 15 Hz and 300 Hz. In Fig. 9 we show the same results for TaylorT4. We find that for mild aligned BH spins with  $\chi_{\text{BH}} \lesssim +0.2$ , TaylorT4 agrees with SEOBNRv2 through a significant portion of the inspiral. For higher or anti-aligned BH spins, the matches fall sharply below 0.7 as more of high frequency orbits are integrated over. The agreement gets restricted to even lower frequencies as the mass-ratio increases, for the entire range of BH spins. From this systematic frequency-dependent discrepancy between PN and SEOBNRv2, we expect that higher order spin-dependent PN corrections to orbital phasing are required for a better PN modeling of the late-inspiral waveform.

Finally, we note that some of the results presented in this section are qualitatively similar to [37], with the differences that (a) we additionally include the recently published spin-orbit tail (3PN) [65] and the next-to-next-to-leading order spin-orbit (3.5PN) contributions [66] in both of the PN models, and (b) we include the SEOBNRv2 and PhenomC models here, both of which are capable of modeling binaries with very high black hole spins  $\chi_{\text{BH}} \simeq +1$ .

## VI. COMPARISON WITH NUMERICAL RELATIVITY SIMULATIONS

In this section, we use our long NR simulations, described in Sec. II, to assess the accuracy of the different model waveforms over the inspiral and merger phases of NSBH binary coalescences.

### A. Mismatch Accumulation for Models

In order to quantify GW model errors over different phases of binary inspiral and merger, we compute matches between each model and NR waveforms over cumulative frequency intervals. The results are shown in Fig. 10–14. Our main results are as follows: (i) Of the two SEOBNR models, SEOBNRv2 reproduces the late-inspiral and merger phases well for NSBH binaries with  $-0.9 \leq \chi_{\text{BH}} \leq +0.6$ . In contrast, the SEOBNRv1 model has an erroneous phase evolution during the late-inspiral phase, causing it to disagree both with the NR simulations and with SEOBNRv2 (cf. Fig. 6) (ii) The pre-merger phasing prescription of PhenomC does not reproduce NR waveforms well, as is confirmed by Ref. [75]. (iii) Of the two PN models we consider here, we found that TaylorT4 is more accurate for aligned BH spins, while TaylorF2 is more accurate for anti-aligned BH spins.

In Figs. 10 and 11, we show the mismatches between the TaylorT4, TaylorF2, PhenomC, SEOBNRv1, and SEOBNRv2 models and our aligned-spin simulations with  $q = m_{\text{BH}}/m_{\text{NS}} = 9.8M_{\odot}/1.4M_{\odot} = 7$ , and  $\chi_{\text{BH}} = \{+0.6, +0.4\}$  (ID SXS:BBH:202, SKS:BBH:203 and SXS:BBH:204, c.f. table I), as a function of the lower (left panels) and upper (right panels) frequency cutoffs in the

match calculation. First, we observe that SEOBNRv2 shows good agreement with NR with mismatches below 0.5% over all 55 – 88 orbits. We also find that SEOBNRv1 agrees with NR over most of the inspiral orbits, but diverges closer to merger, with mismatches reaching 10% when considering the last few orbits. Therefore, we conclude that the disagreement between the two SEOBNR models for positive aligned spins that was seen in Fig. 6 stems from the phasing errors of SEOBNRv1. Next, we find that the PhenomC model agrees well with the first few tens and the last few orbits of the NR waveforms only. It accumulates *significant* phase errors in a narrow frequency band around 130 – 150 Hz, with mismatches rising above 10%. This explains the pattern of mismatch accumulation we observed in the middle panel of Fig. 7 and reaffirms our conclusion that the pre-merger phasing prescription of PhenomC needs to be revisited for NSBH parameters [75]. We also find that both TaylorF2 and TaylorT4 (c.f. right panels of Fig. 10 and 11) agree with NR well up to the last 15 or so pre-merger orbits. Closer to merger, their mismatches smoothly rise to 10%, which is expected as the PN approximation degrades with increasing binary velocity. In addition, we find that TaylorT4 agrees with these NR waveforms to higher frequencies than TaylorF2, which is consistent with Fig. 5, where we show that TaylorT4 best agrees with SEOBNRv2 for aligned, moderate BH spins. Finally, we note that the bottom row of Fig. 11 shows the comparison of different approximants with a shorter NR simulation (ID SXS:BBH:203, starting frequency  $\sim 80$  Hz) with the same physical parameters as a longer simulation (ID SXS:BBH:204, starting frequency  $\sim 60$  Hz). Therefore, the results for this simulation confirm those shown for the longer simulation (same figure, top row) for frequencies above 80 Hz.

Next, we consider the case of NSBH binaries with anti-aligned BH spins. We show the mismatches between approximants and NR waveforms corresponding to  $q = m_{\text{BH}}/m_{\text{NS}} = 9.8M_{\odot}/1.4M_{\odot} = 7$  and  $\chi_{\text{BH}} = \{-0.4, -0.6\}$  (ID SXS:BBH:205–207), in Fig. 12 and Fig. 13, respectively. We find that SEOBNRv2 shows the best agreement with NR, with mismatches below 0.2% across all orbits. SEOBNRv1 *monotonically* accumulates increasing mismatches when we lower the lower frequency cutoff and appears to do the same over the later orbits when we increase the upper frequency cutoff, suggesting a phasing mismatch between the inspiral and merger portions of the waveform. Therefore, we conclude that the disagreement between the two SEOBNR models for anti-aligned spins that was seen in Fig. 6 stems from the phasing errors of SEOBNRv1. Similar to the aligned-spin cases, the PhenomC model agrees well with NR over the first few tens and the last couple of orbits, with mismatches below 1%, but accumulates large mismatches (10%) over a relatively narrow frequency range around 110 Hz. All of these observations are qualitatively similar to the aligned-spin cases. Lastly, we find that TaylorF2 shows excellent agreement with our NR waveforms over the first 60 – 65 orbits, with mismatches below 1%. It gradually diverges during the last 5 pre-merger orbits, with high mismatches, which is consistent with the right panel of Fig. 4. TaylorT4, on the other hand, performs worse, with mismatches accumulating earlier on and rising to 10%. The

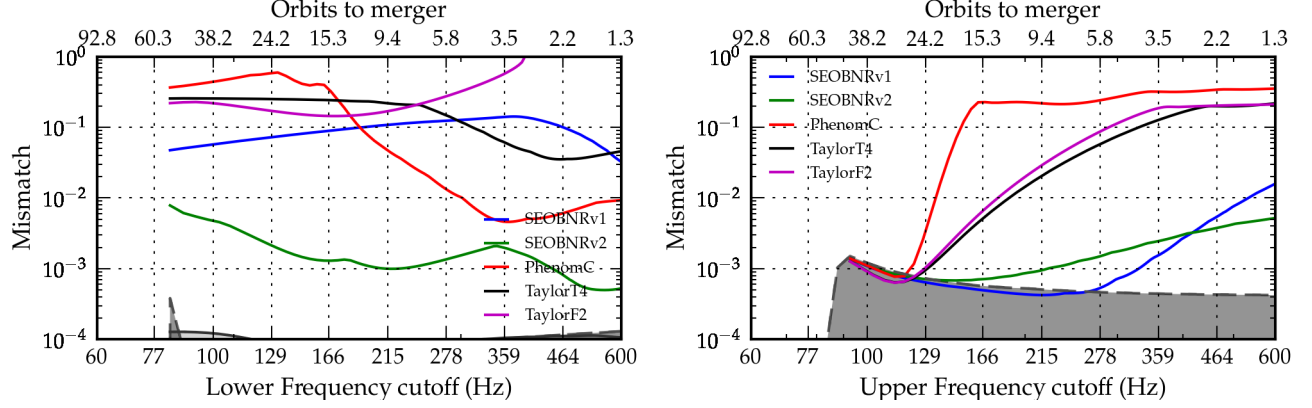


FIG. 10. For a NSBH binary with  $q = m_{\text{BH}}/m_{\text{NS}} = 9.8M_{\odot}/1.4M_{\odot} = 7$  and  $\chi_{\text{BH}} = +0.6$ , these figures show the mismatch of TaylorF2, TaylorT4, SEOBv1, SEOBv2 and PhenomC waveforms against our simulation ID SXS:BBH:202 (see Table I) as a function of the lower (left) and upper (right) frequency cutoff on the overlap integral. The NR waveform starts from GW frequency  $f_0 \simeq 80$  Hz. The dashed curve with dark grey shading (in both panels) shows mismatches because of the tapering and high-pass filtering of NR waveforms, which we do to reduce Gibbs phenomena and spectral leakage upon Fourier transformation. Because of the width of the tapering window, we begin filtering at 82.5 Hz. The solid curve with light grey shading (only barely visible at the bottom of the left panel and below the range of mismatches shown in the right panel) shows the mismatches between NR waveforms at the highest and second-highest available numerical resolutions.

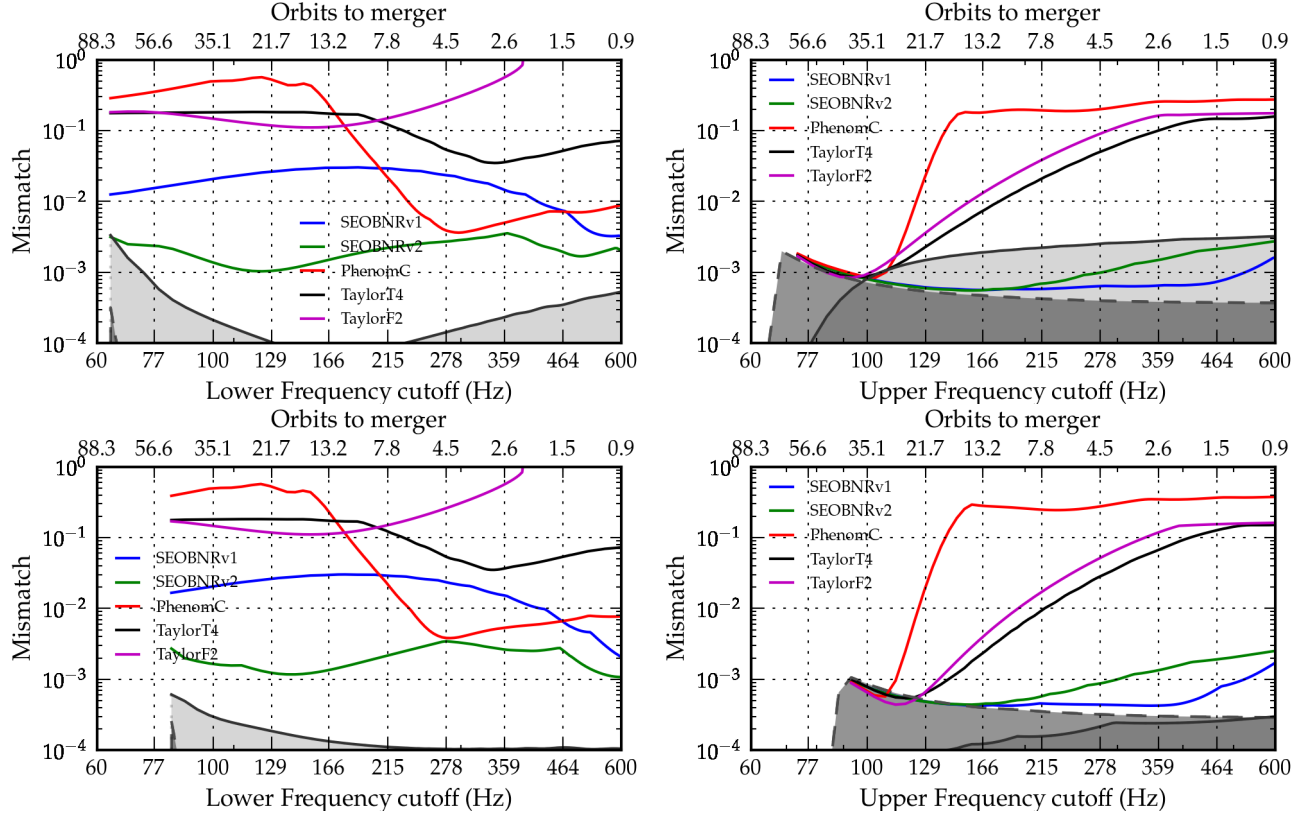


FIG. 11. The top two panels of this figure are similar to the two panels of Fig. 10, with the difference that the system considered here has  $q = m_{\text{BH}}/m_{\text{NS}} = 9.8M_{\odot}/1.4M_{\odot} = 7$ ,  $\chi_{\text{BH}} = +0.4$ , and starts at GW frequency  $\simeq 60$  Hz. This corresponds to simulation ID SXS:BBH:204 (see Table I). The bottom two panels are similar to the top two with the difference that these correspond to simulation ID SXS:BBH:203, which has the same physical parameters as ID SXS:BBH:203 but a higher starting GW frequency, i.e.  $\simeq 80$  Hz. Because of the width of the tapering windows, we begin filtering at 63.5 Hz and 83 Hz, respectively.



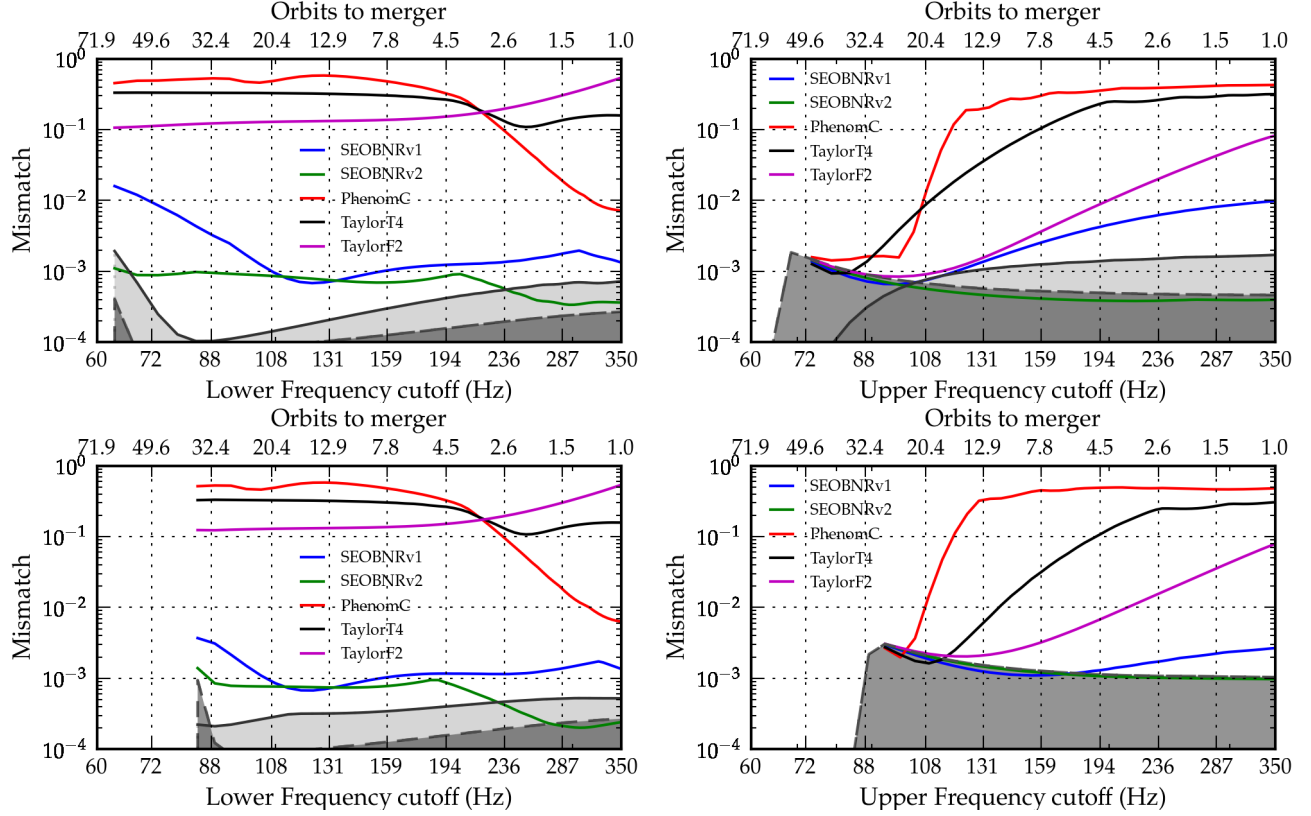


FIG. 12. The top two panels of this figure are similar to the two panels of Fig. 10, with the difference that the system considered here has  $q = m_{\text{BH}}/m_{\text{NS}} = 9.8M_{\odot}/1.4M_{\odot} = 7$ ,  $\chi_{\text{BH}} = -0.4$ , and starts at GW frequency  $\simeq 60$  Hz. This corresponds to simulation ID SXS:BBH:206 (see Table I). The bottom two panels are similar to the top two with the difference that these correspond to simulation ID SXS:BBH:205, which has the same physical parameters as ID SXS:BBH:206 but a higher starting GW frequency, i.e.  $\simeq 80$  Hz. Because of the width of the tapering windows, we begin filtering at 63.5 Hz and 84 Hz, respectively.

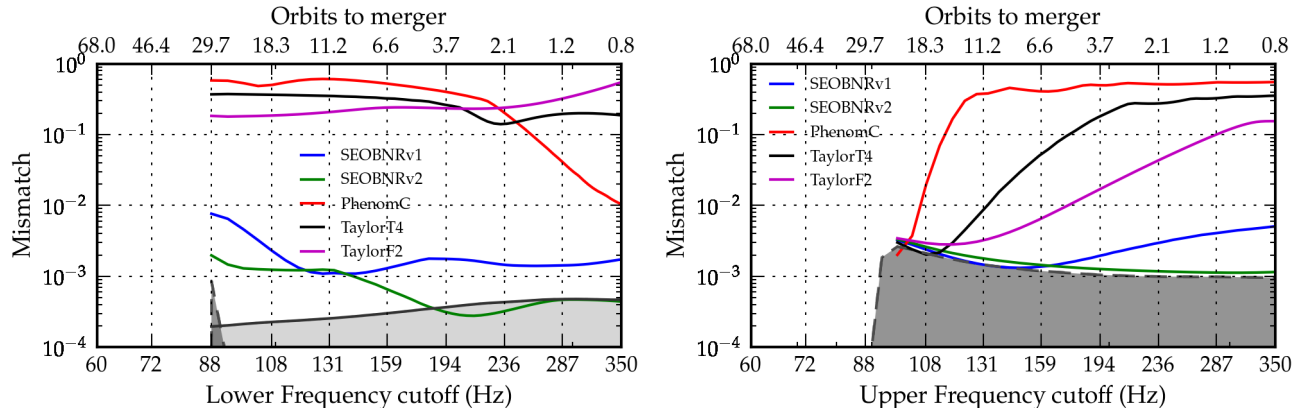


FIG. 13. These figures are similar to the two panels of Fig. 10, with the difference that the system considered here has  $q = m_{\text{BH}}/m_{\text{NS}} = 9.8M_{\odot}/1.4M_{\odot} = 7$ ,  $\chi_{\text{BH}} = -0.6$ , and starts at GW frequency  $\simeq 80$  Hz. This corresponds to simulation ID SXS:BBH:207 (see Table I). Because of the width of the tapering window, we begin filtering at 88 Hz.

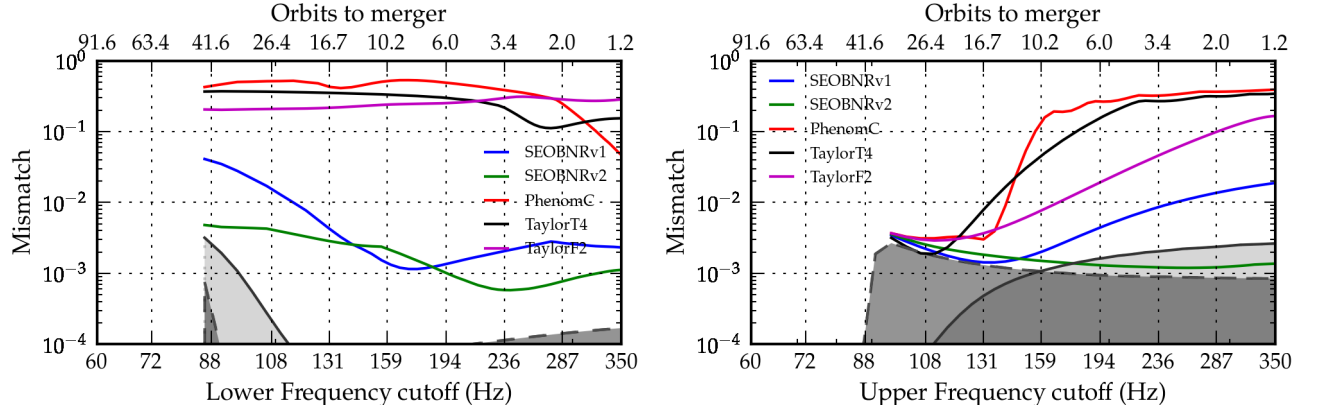


FIG. 14. These figures are similar to the two panels of Fig. 10, with the difference that the system considered here has  $q = m_{\text{BH}}/m_{\text{NS}} = 7M_{\odot}/1.4M_{\odot} = 5$ ,  $\chi_{\text{BH}} = -0.9$ , and starts at GW frequency  $\simeq 80$  Hz. This corresponds to simulation ID SXS:BBH:208 (see Table I). Because of the width of the tapering window, we begin filtering at 86 Hz.

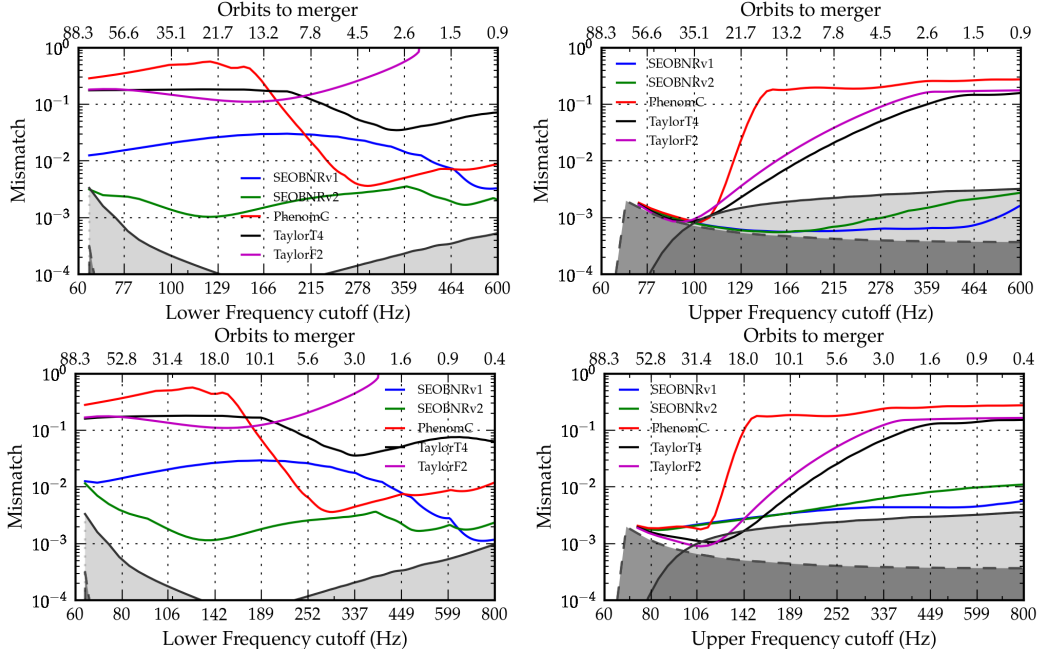


FIG. 15. The top panels in this figure are reproductions of the top two panels of Fig. 11, and are shown here for direct comparison. The bottom two panels show identically computed quantities, with the only difference from the top two being that the NR waveform used corresponds to the second-highest numerical resolution instead of the highest. The case shown here has the highest mismatches between the highest and second-highest resolution NR waveforms, and therefore serves as a conservative example of the robustness of our results to NR errors.

bottom row of Fig. 12 shows identical comparisons with the shorter NR waveform ID SXS:BBH:205 with the same physical parameters as ID SXS:BBH:206. As in the aligned case, these panels agree with and provide a confirmation for the results shown in the top row of the figure, for frequencies above 80 Hz.

Finally, we compare different approximants with NR simulation ID SXS:BBH:208, which has a smaller mass-ratio  $q = 5$  but the most extremal BH spin of all the cases we consider, with  $\chi_{\text{BH}} = -0.9$ . Compared to the above two anti-aligned spin cases, we find that the SEOBNRv1 mismatches rise to 5%, indicating that the phasing errors of SEOBNRv1

get worse with BH spin magnitude. SEOBNRv2 still reproduces the NR waveform the best, while PhenomC and both PN approximants show similar patterns to the  $q = 7$  anti-aligned spin cases.

Overall, we conclude that the more recently calibrated SEOBNRv2 [67] model reproduces the late-inspiral and merger phases well for NSBH binaries with  $-0.9 \leq \chi_{\text{BH}} \leq +0.6$ . This model was calibrated to 8 non-spinning and 30 non-precessing spinning simulations with mass-ratios up to  $q = 8$ , and most of the NSBH systems we consider here are within the calibration range of the model. Therefore, we conclude that SEOBNR performs well when interpolated within

its calibration range. We also conclude that PhenomC does not reproduce NR waveforms well, and its NR-calibrated portion needs to be revisited [75]. Of the two PN models we consider here, TaylorT4 and TaylorF2, we found that the former has better accuracy for aligned-spin binaries, while the latter is more accurate for the case of anti-aligned BH spins. These patterns, however, are likely coincidental.

Finally, note that in detection searches there is an additional degree of freedom corresponding to the maximization of the SNR over the intrinsic waveform parameters. We investigate the suitability of the GW models considered here as detection templates in Sec. VII.

### B. Impact of numerical errors in NR simulations

Fig. 2 shows that some of the NR simulations (especially the ones with  $\chi_{\text{BH}} = \pm 0.4$ ) do not show explicit convergence with an increase in numerical grid resolution. Therefore, one might question the effect of the errors in the numerical waveforms that arise because of a finite grid resolution. In order to quantify this, in this section, we repeat the overlap calculations for the  $\chi_{\text{BH}} = +0.4$  configuration, using the NR waveform produced at the second-highest grid resolution. We choose this configuration because it exhibits the highest NR(highest resolution)-NR(next-to-highest resolution) mismatches, as shown by the solid line bounding the light grey region in Fig. 11. We show the results in the bottom row of Fig. 15. The top row in the figure is a reproduction of the top row of Fig. 11, which uses the NR waveform produced at the highest grid resolution. From the left two panels, we first notice that the PhenomC, TaylorT4 and TaylorF2 mismatches are sufficiently large for the variations because of NR waveform differences to be inconsequential. Further, for both SEOBNRv1 and SEOBNRv2, we find a small change in the mismatches near the left and the right edge of the two left panels. These fluctuations are entirely consistent with the value of the NR-NR mismatch (shown by the solid grey line), when we apply the triangle inequality to the square roots of the SEOBNR-NR and NR-NR mismatches (see Sec. III of Ref. [76] for a brief discussion on manipulation of waveform mismatches arising from independent sources). The same is true when we compare the two right panels in Fig. 15. In this case, the changes visible in the SEOBNR-NR mismatches are below the upper bound set by adding the square roots of the SEOBNR-NR and NR-NR mismatches.

We therefore conclude that the fluctuations in the mismatches computed in the previous subsection are within the error bounds set by comparing NR waveforms at the highest and second-highest numerical grid resolutions. These bounds are shown explicitly in light grey shading bounded by solid lines in all panels of Fig. 10-13. As these fluctuations remain below 0.3% in all cases, our conclusions remain robust to NR waveform errors.

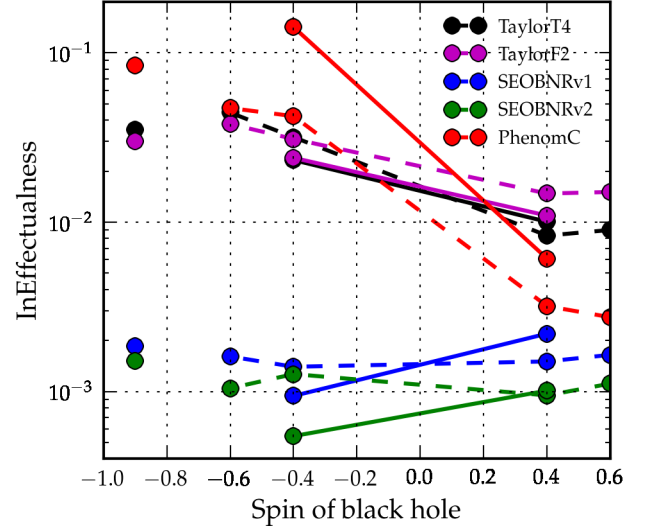


FIG. 16. In this figure, we show the ineffectualness of different waveform approximants against our NR waveforms, as a function of black hole spin. Dashed lines join points corresponding to the cases where the NR waveform starts at  $\sim 80$  Hz (ID: 01, 02a, 03a, 04), while the solid lines correspond to the cases where the NR waveform starts at  $\sim 60$  Hz (ID: 02b, 03b). The isolated points correspond to the  $q = 5$  simulation (ID: 5). We find that SEOBNRv2 consistently recovers the highest fraction ( $\geq 99.8\%$ ) of the optimal SNR when optimizing over intrinsic binary parameters. SEOBNRv1 is also fairly effectual. The Taylor approximants recover 97 – 98% of the SNR and noticeably more for the longer NR waveforms (for fixed binary parameters). This is the expected trend, as longer waveforms extend to lower frequencies, where the PN approximation is better. PhenomC is effectual against NR for  $\chi_{\text{BH}} \geq 0$ , recovering  $\geq 99\%$  of the SNR. For anti-aligned spins, however, its effectualness was found to be low and decreasing with increasing NR waveform length.

## VII. EFFECTUALNESS AND PARAMETER BIAS

While accurate parameter estimation requires that waveform models be faithful to the true signal for given binary parameters, detection searches allow for the additional degree of freedom of maximizing the SNR over intrinsic binary parameters. With this freedom, intrinsic waveform model errors can be compensated by slight shifts in the physical parameters. As a result, a GW signal will be better matched with a template waveform with slightly incorrect physical parameters. In this section, we investigate the recovery of SNR using different approximants and the associated biases in the recovered maximum likelihood estimates for binary masses and spins. We take all of our NR waveforms, produced at the highest numerical resolution, and compute their overlaps against 500,000 modeled waveforms with physical parameters in the vicinity of the true NR parameters. We compute waveform overlaps integrating from the starting frequency of the simulation in question, up to the Nyquist frequency corresponding to the waveform sampling rate.



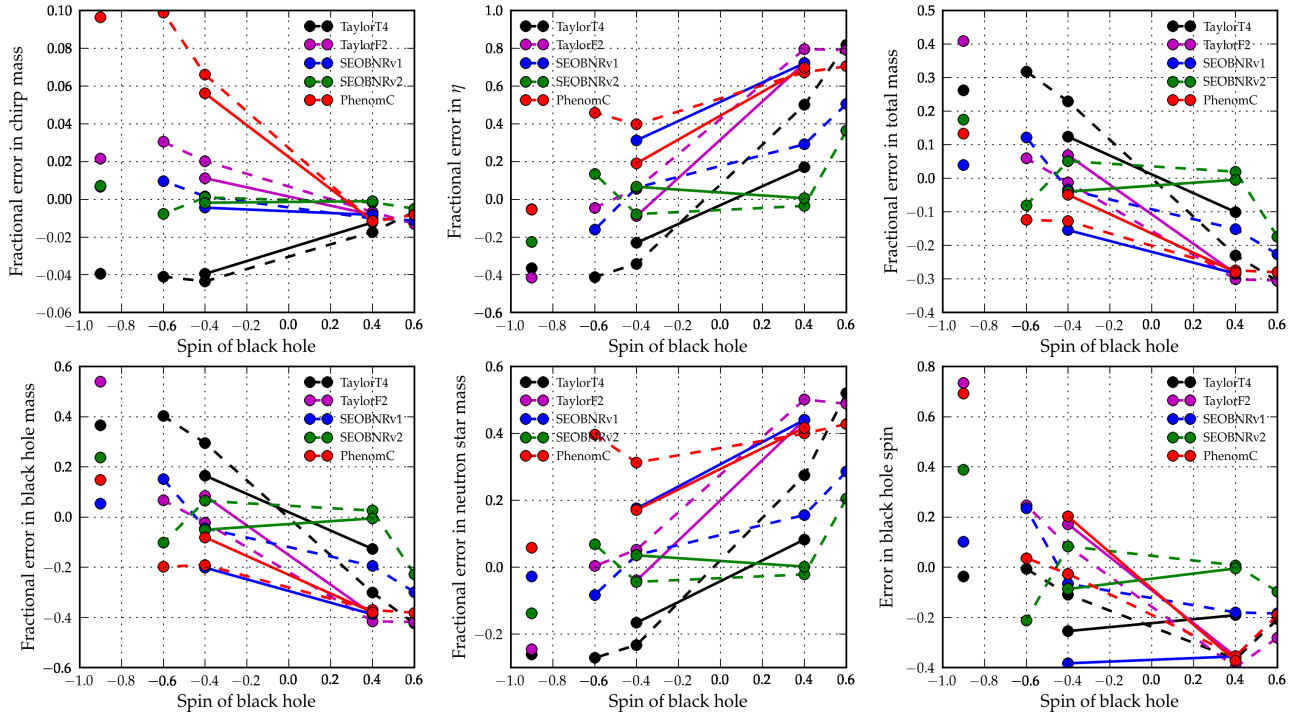


FIG. 17. These figures show the fractional error in the recovered maximum likelihood parameters as a function of black hole spin, except for black hole spin for which the actual error value is shown. Each approximant is denoted with a unique color. As in Fig. 16, dashed lines join points corresponding to NR waveforms that start at  $\sim 80$  Hz (ID: 01, 02a, 03a, 04), while the solid lines correspond to the ones starting at  $\sim 60$  Hz (ID: 02b, 03b). The isolated points correspond to the  $q = 5$  simulation (ID: 5). While the left-to-right trends show us the effect of component spin, comparing dashed and solid lines show us the effect of including more inspiral cycles.

In Fig. 16 we show the fractional loss in SNR, or the ineffectualness of approximants, as a function of BH spin. The  $q = 7$  cases are connected with straight lines, while the single  $q = 5$  case is shown by a point. Each approximant is shown with a different color. Solid and dashed lines join points corresponding to ID 2a, 3a and ID 1, 2b, 3b, 4, respectively. Detection searches use banks of templates that correspond to a grid in the parameter space, and the SNR loss due to the discreteness of the grid will be *in addition* to those shown in this figure. We find that both EOB models recover more than 99.5% of the optimal SNR for both aligned and anti-aligned BH spins, despite different faithfulness. This is a good example of a shift in waveform parameters compensating for model phasing errors. For aligned-spin cases, both PN approximants as well as PhenomC are effectual with SNR recovery above 98%. For all of the anti-aligned spin cases, however, we found relatively low SNR recovery using PN approximants, which is to be expected as anti-aligned spin binaries merge at lower frequencies than aligned-spin cases and therefore have relatively less signal power in the inspiral cycles above a given physical frequency (here 60 – 80 Hz). PhenomC also shows significantly low effectualness for anti-aligned systems, recovering  $\leq 96\%$  of the SNR for  $q = 7$  cases and 91.5% for the  $q = 5$ ,  $\chi_{\text{BH}} = -0.9$  case. We therefore conclude that (a) both SEOBNR models are sufficiently accurate to model NSBH templates in aLIGO detection searches, and (b) PN approximants are also viable for use as filter templates for *aligned*-

spin NSBH systems.

In Fig. 17 we show the fractional difference between the parameters that maximize the SNR recovery for each of the approximants, i.e. the maximum likelihood parameters, and the true physical parameters of the system. Table II lists the same for the IMR approximants, and Table III for the inspiral-only approximants. These differences quantify the systematic bias intrinsic to each approximant. From the top left panel of Fig. 17, we observe that as the number of waveform cycles increases (monotonically with BH spin), so does the accuracy of the recovered chirp mass. For aligned spins, all approximants but SEOBNRv2 converge at a systematic  $-1\%$  bias in chirp mass recovery. SEOBNRv2 shows a smaller ( $< 0.8\%$ ) bias in chirp mass for all BH spins. In the top center panel of Fig. 17, we show the bias in mass-ratio recovery. The spin-mass-ratio degeneracy that enters at the sub-leading order in PN phasing is manifest here, and for PN models, we find i) a larger bias in  $\eta$  for aligned spins that increases with the spin magnitude and ii) a smaller (or negative) bias for anti-aligned spins. We see a similar trend for the IMR approximants, with SEOBNRv2 showing the smallest systematic bias. We also show biases in other binary mass combinations, total mass in the top right panel, BH mass in the bottom left, and NS mass in the bottom center. These show that none of the individual masses or their sum are nearly as accurately measured as the chirp mass of the binary. Additionally, the mass of the smaller component, here the NS, is slightly more biased than for the more

SEOBNRv1					
Actual $S_{\text{BH}}$	$\mathcal{M}_c$	$\eta$	$m_1$	$m_2$	$S_{\text{BH}}$
0.6	-1.12%	50.45%	-29.9%	28.6%	-0.184
0.4 (80Hz)	-1.02%	29.1%	-19.5%	15.6%	-0.180
0.4 (60Hz)	-0.82%	72.1%	-38.8%	44.1%	-0.355
-0.4 (80Hz)	0.16%	6.19%	-4.40%	3.67%	-0.066
-0.4 (60Hz)	-0.44%	31.3%	-20.2%	17.6%	-0.382
-0.6	0.97%	-16.1%	15.1%	-8.29%	0.234
-0.9 ( $q = 5$ )	0.66%	-5.2%	5.3%	-2.7%	0.102
SEOBNRv2					
Actual $S_{\text{BH}}$	$\mathcal{M}_c$	$\eta$	$m_1$	$m_2$	$S_{\text{BH}}$
0.6	-0.49%	36.3%	-22.8%	20.5%	-0.0966
0.4 (80Hz)	-0.16%	-3.48%	2.57%	-2.13%	0.00808
0.4 (60Hz)	-0.10%	0.54%	-0.51%	0.21%	0.00444
-0.4 (80Hz)	0.10%	-7.84%	6.48%	-4.35%	0.0836
-0.4 (60Hz)	-0.18%	6.64%	-5.03%	3.58%	-0.0864
-0.6	-0.77%	13.5%	-10.2%	6.87%	0.234
-0.9 ( $q = 5$ )	0.7%	-22.7%	23.7%	-13.7%	0.387
PhenomC					
Actual $S_{\text{BH}}$	$\mathcal{M}_c$	$\eta$	$m_1$	$m_2$	$S_{\text{BH}}$
0.6	-0.82%	70.5%	-38.1%	42.8%	-0.191
0.4 (80Hz)	-1.18%	67.3%	-37.0%	40.0%	-0.353
0.4 (60Hz)	-1.14%	69.6%	-38.0%	41.7%	-0.373
-0.4 (80Hz)	6.59%	39.7%	-19.1%	31.3%	-0.0259
-0.4 (60Hz)	5.61%	19.1%	-8.06%	17.1%	0.202
-0.6	9.90%	45.9%	-19.8%	39.7%	0.0366
-0.9 ( $q = 5$ )	9.6%	-5.4%	14.8%	5.8%	0.693

TABLE II. In this table we list the fractional error in the recovered maximum likelihood parameters for different IMR approximants. For BH spin, we give the actual difference between maximum likelihood and true parameter.

TaylorT4					
Actual $S_{\text{BH}}$	$\mathcal{M}_c$	$\eta$	$m_1$	$m_2$	$S_{\text{BH}}$
0.6	-0.67%	81.9%	-42.4%	52.1%	-0.207
0.4 (80Hz)	-1.73%	50.0%	-30.1%	27.5%	-0.366
0.4 (60Hz)	-1.23%	16.92%	-12.7%	8.31%	-0.191
-0.4 (80Hz)	-4.35%	-34.2%	29.5%	-23.2%	-0.109
-0.4 (60Hz)	-3.95%	-23.0%	16.5%	-16.6%	-0.254
-0.6	-4.09%	-41.1%	40.2%	-27.1%	-0.00606
-0.9 ( $q = 5$ )	-3.94%	-36.5%	36.6%	-26%	-0.0374
TaylorF2					
Actual $S_{\text{BH}}$	$\mathcal{M}_c$	$\eta$	$m_1$	$m_2$	$S_{\text{BH}}$
0.6	-1.30%	79.1%	-41.8%	48.9%	-0.281
0.4 (80Hz)	-0.67%	79.6%	-41.5%	50.1%	-0.398
0.4 (60Hz)	-0.82%	72.1%	-38.8%	44.1%	-0.355
-0.4 (80Hz)	2.02%	5.61%	-2.20%	5.27%	0.0828
-0.4 (60Hz)	1.12%	-8.82%	8.42%	-3.94%	0.172
-0.6	3.04%	-4.53%	6.74%	0.40%	0.247
-0.9 ( $q = 5$ )	2.16%	-41.5%	54%	-24.6%	0.735

TABLE III. This table is identical to Table II, but for inspiral-only approximants.

massive component (here the BH). Finally, the bottom right panel of the same figure shows the bias in recovered values of black hole spin. We observe a systematic underestimation of BH spin when it is aligned with the orbit, and smaller underestimation or overestimation when it is anti-aligned. Both of

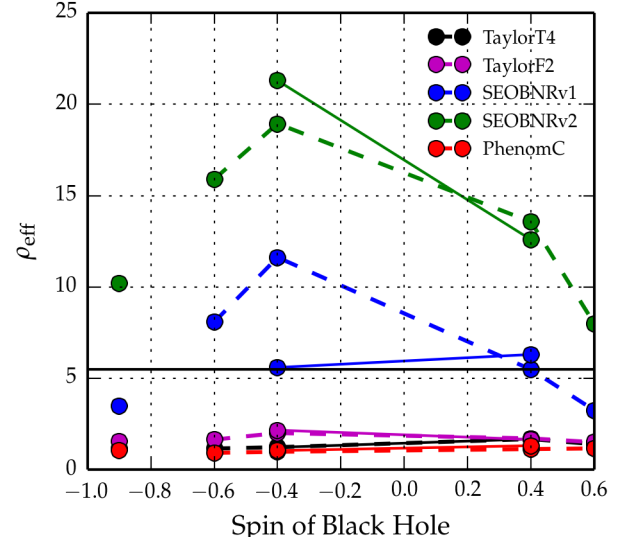


FIG. 18. In this figure, we show the lowest SNR value below which a modeled waveform (using the respective approximant) with the same parameters as the true signal waveform will be indistinguishable from the true signal waveform. Here, the true signal waveform is represented by the corresponding NR waveform. We use the criterion proposed in Ref. [49] for this calculation. As in Fig. 16, solid lines correspond to the two longer simulations that start at 60 Hz, dashed lines are for the shorter simulations that start at 80 Hz, and the isolated points correspond to the  $q = 5$  simulation (ID: 5). For all but SEOBNRv2 (and marginally SEOBNRv1), this threshold is below the SNR cutoff ( $= 5.5$ , shown by horizontal black line) employed by past LIGO-Virgo searches, and therefore their use would likely degrade the extraction of information from detector data.

these patterns are exacerbated with BH spin magnitude.

Overall, we found SEOBNRv2 to have the smallest systematic biases in parameter recovery. Therefore, we recommend its use in aLIGO parameter estimation efforts focused on non-precessing NSBH binaries.

Having ascertained the systematic parameter biases that are applicable in the limit of high SNR, we ask the question: how loud does an incoming GW signal have to be before a modeled waveform with the same parameters is distinguishable from the true, measured waveform? Ref. [49] proposed the criterion:  $(\delta h | \delta h) < 1$ , where  $\delta h \equiv h^{\text{true}} - h^{\text{approx}}$ , which is sufficient for proving the indistinguishability of the modeled waveform  $h^{\text{approx}}$  from the true signal  $h^{\text{true}}$ . We use it to calculate the effective SNR  $\rho_{\text{eff}}$  below which different approximants are indistinguishable from true (NR) waveforms, and show it in Fig. 18 as a function of black hole spin, for all  $q = 7$  and  $q = 5$  cases. We immediately observe that for TaylorF2, TaylorT4, and PhenomC, the SNR threshold for distinguishability is below what is chosen as the single detector SNR lower cutoff in LIGO searches ( $= 5.5$ ) and therefore using these approximants would likely degrade scientific measurements. For SEOBNRv1, inclusion of more inspiral cycles for anti-aligned spin cases ID 3,  $b$  cause a drop in  $\rho_{\text{eff}}$  from 12 – 6. This is consistent with Fig. 12 which shows that SEOBNRv1 monotonically diverges from the reference NR waveform(s) when more of inspiral cycles are considered. For

aligned-spin cases, we find that SEOBNRv1 is always distinguishable from a real signal with SNR above the lower cutoff for aLIGO searches. SEOBNRv2 is indistinguishable from true waveforms to fairly high SNRs  $\sim 15 - 20$  for anti-aligned spins, but this threshold lowers when we consider the longer, aligned-spin cases.

Lastly, we note that the SNR in consideration here is integrated from the starting frequency of the NR waveform in question, i.e.  $\sim 60$  or  $80$  Hz, and corresponds to about  $50 - 70\%$  of the total SNR accumulated over the entire aLIGO frequency band starting from  $15$  Hz. These results are therefore likely to be pessimistic for PN models, since these models do better at lower frequencies, where PN is more accurate.

### VIII. CONCLUSIONS

With the first observations of the Advanced LIGO and Virgo detectors imminent, rapid development of data analysis methods is underway within the LIGO Scientific Collaboration and the Virgo Collaboration. Gravitational-wave astronomers are shaping matched-filtering-based targeted searches for neutron star - black hole binaries. As a step forward from most of earlier LIGO-Virgo searches (which used non-spinning waveforms as templates, e.g. [24–27]), Advanced LIGO searches plan to employ aligned-spin waveforms as templates. This is motivated towards increasing the sensitivity of the searches for binaries with spinning components. Recent work has shown that even if the component spins are not aligned to the orbital angular momentum and result in orbital precession, aligned-spin waveform templates would likely have significantly better sensitivity towards such systems than non-spinning waveform templates [33].

Recent progress in numerical relativity has allowed for faster and more accurate general-relativistic numerical simulations of inspiraling black holes, including the effect of component spin [54]. With these advances, more and longer simulations of compact binary motion have become possible [77]. While the possibility of using numerical relativity waveforms directly as search templates has been demonstrated [76], Bayesian parameter estimation efforts will require the ability to generate template waveforms for arbitrary source parameters. This is computationally prohibitive with the current NR technology, and therefore approximate waveform models are indispensable. Using strong-field information from numerical relativity, Effective-One-Body (EOB) and phenomenological (Phenom) models have been developed and calibrated to accurately model the late-inspiral motion of compact binaries all the way through merger. The NR input here has been critical, since the post-Newtonian expressions that form the basis of all IMR models are perturbative expansions in the invariant velocity  $v/c$ , which become inaccurate in the strong field, rapid motion regime. While the Phenom models are closed-form in frequency domain and therefore the least expensive to generate, reduced-order methods have been recently applied to the EOB family to mitigate their computational cost [78].

In this paper, we present 7 new NR simulations, 6 with

$q = m_1/m_2 = 7$  and black hole spins  $\chi_{\text{BH}} = \{\pm 0.4, \pm 0.6\}$ , and 1 with  $q = 5$  and  $\chi_{\text{BH}} = -0.9$ . The spin of the smaller object (a black hole representing the neutron star) is held at 0. For  $\chi_{\text{BH}} = \pm 0.4$ , we perform two simulations each, one starting at a gravitational-wave frequency of  $60$  Hz and the other starting at  $80$  Hz (corresponding to a total mass of  $1.4M_\odot + 7 \times 1.4M_\odot = 11.2M_\odot$ ). These span  $36 - 88$  pre-merger orbits. For all other parameter values, our simulations start close to  $80$  Hz when scaled to appropriate NSBH masses (cf. Table I). Using these simulations, we study the accuracy of different waveform approximants and their effectualness as models for search and parameter estimation templates for the Advanced detector era.

Our investigation of the faithfulness of two inspiral-merger-ringdown models and two inspiral-only PN models shows that both PN models become increasingly unfaithful with increasing BH spin magnitudes as well as with binary mass ratio, with overlaps falling below  $50\%$ . This is consistent with a similar study [37] and is indicative of the breakdown of the PN approximation with increasing binary velocity. We find that PhenomC disagrees in an even larger portion of the parameter space with SEOBNRv2, with overlaps above  $0.9$  for near-equal mass binaries with spin magnitude below  $0.3$ . Somewhat surprisingly, we also find that the two SEOBNR models diverge *significantly* for anti-aligned BH spins. Next, we investigate the GW frequency dependence of these model disagreements to disambiguate the portion of the binary coalescence process, that each model fails to capture accurately. As expected, the PN models describe the inspiral well but break down closer to merger. We found that PhenomC accumulates most of the mismatch against SEOBNRv2 close to the frequencies where it switches its phase prescription from one piece of a piece-wise continuous function to another. Lastly, for aligned spins, SEOBNRv1 accumulates phase differences close to merger, but for anti-aligned spins it agrees with SEOBNRv2 close to merger, with most of its mismatch being accumulated earlier on during the late inspiral. We present these results in detail in Sec. V.

When we study the mismatch accumulation of GW models as a function of frequency, we find that the PN models are faithful at the lower frequencies of our NR waveforms, and diverge close to merger. We find that PhenomC reproduces NR waveforms accurately during the last  $2 - 5$  and first  $20 - 30$  orbits, but accumulates significant mismatches over a span of  $\sim 20$  orbits around  $100$  Hz. For SEOBNRv1, we find that (a) for aligned-spin binaries, it slowly accumulates phase error over the last  $\sim 5$  orbits with mismatches rising to  $10\%$ , but agrees well earlier on, but (b) for anti-aligned binaries, it agrees well with NR during the last  $10 - 20$  orbits and diverges *monotonically* when more inspiral orbits are included, with mismatches rising to  $2\%$ . In contrast, SEOBNRv2 reproduced all of our NR waveforms well, throughout the probed frequency range, with mismatches below  $1\%$ . We summarize these results in Sec. VI.

Further, we study the effectualness of these models as detection templates. Detection searches allow for the additional freedom of maximizing the match of template with signal over the intrinsic parameters of the templates, allowing for partial



compensation of modeling errors. Using this freedom, we computed the mass-and-spin optimized overlaps between our set of numerical waveforms and those generated using different waveform approximants. For BH spins aligned with the orbital momentum, all models are effectual against our NR waveforms, with SNR recovery above 98%. For anti-aligned BH spins, we find that both PN models are less effectual, with SNR recovery dropping below  $\lesssim 96.5\%$ . This is expected, since our NR waveforms have fewer inspiral orbits for anti-aligned spins, even though they span similar frequency ranges. We find that PhenomC recovers the lowest SNRs (below 90 – 95%, depending on spin) for anti-aligned spins. We find that both SEOBNR models recover more than 99.8% of the optimal SNR when maximized over physical parameters. Therefore, we recommend using SEOBNR models to model non-precessing templates in aLIGO detection searches. We also note that the unpublished PhenomD model (an improvement over PhenomC) has shown promising results in terms of accurately capturing the merger waveforms for high mass-ratio non-precessing binaries [79], and would therefore be another suitable candidate for modeling search and parameter estimation templates in aLIGO era.

Finally, we also investigate the systematic bias in maximum likelihood recovered parameters that GW models will incur if used to model parameter estimation templates. We find that while the chirp mass is recovered increasingly and very accurately (within a percent) with increasing number of binary orbits in detector frequency band, the spin-mass-ratio degeneracy makes accurate determination of other parameters more difficult. For mass-ratio, we find that TaylorT4, TaylorF2, PhenomC, and SEOBNRv1 have a 20 – 50 + % bias, with SEOBNRv2 relatively the most faithful to NR with a 2 – 38% bias. We also find that the models consistently underestimate BH spins for aligned-spin binaries, and overestimate (or slightly underestimate) it for anti-aligned binaries. Overall, we find SEOBNRv2 to be the most faithful approximant to NR. As these biases are applicable in the high SNR limit, we also investigate the SNR limit below which different approximants are essentially indistinguishable from NR waveforms [49]. We find that for PN and Phenom models, this is never the case for signals with SNRs above 5; but up to SNR  $\rho_{\text{eff}} \sim 10 - 22$  (depending on spin), any further increase in the accuracy of SEOBNRv2 will not affect the extraction of scientific information from detector data. We describe these results in Sec. VII. Therefore, for NSBH binaries with moderate spins, parameter estimation efforts will benefit from using SEOBNRv2 templates in aLIGO era. However, given the drop in accuracy of the SEOBNRv1 model outside its range of calibration, we also recommend further investigating SEOBNRv2 at more extremal component spins, and we recommend trusting SEOBNRv2 only within its calibration range.

We note that we ignore a good fraction (35 – 45%, depending on BH spin) of the signal power by considering only frequencies above 60 – 80 Hz. Therefore, our results are accurate in the high-frequency limit and are likely to be pessimistic

for the PN-based inspiral-only models. We plan to extend the study to lower frequencies in future work. We also note that there is tremendous ongoing effort to model the effect of the tidal distortion of neutron stars during NS-BH mergers [46]. They are expected to be measurable with aLIGO detectors [45]. However, matter effects affect binary phasing at 5+PN order, while there are lower order unknown spin dependent terms in PN phasing whose lack of knowledge will have a larger impact on the detection problem [80]. This motivates our choice to ignore neutron star matter effects in our numerical simulations, and instead treating the neutron stars as low-mass black holes. We have also ignored the effect of the possible tidal disruption of NS in this study, and leave its detailed analysis to future work. However, since NS disruption affects NSBH waveforms only at very high ( $\gtrsim 1.2$  kHz) frequencies [47] where aLIGO has significantly reduced sensitivity, ignoring it is unlikely to affect the accuracy of our analysis. Finally, we note that we consider only the dominant  $l = \pm m = 2$  waveform multipoles in this study, since (i) other multipoles have much smaller (by orders of magnitude) contribution to the SNR, and (ii) none of the IMR models considered here include sub-dominant modes.

## ACKNOWLEDGMENTS

We thank the Gravitational-Wave group at Syracuse University for productive discussions. DAB and PK are grateful for hospitality of the TAPIR group at the California Institute of Technology, where part of this work was completed. PK acknowledges support through the Ontario Early Research Award Program and the Canadian Institute for Advanced Research. DAB and SB are supported by NSF awards PHY-1404395 and AST-1333142; NA and GL are supported by NSF award PHY-1307489 and by the Research Corporation for Science Advancement. KB, MS, and BSz are supported by the Sherman Fairchild Foundation and by NSF grants PHY-1440083 and AST-1333520 at Caltech. Simulations used in this work were performed with the `SpEC` code [50]. Calculations were performed on the Zwicky cluster at Caltech, which is supported by the Sherman Fairchild Foundation and by NSF award PHY-0960291; on the NSF XSEDE network under grant TG-PHY990007N; on the Syracuse University Gravitation and Relativity cluster, which is supported by NSF awards PHY-1040231 and PHY-1104371 and Syracuse University ITS; on the Orca cluster supported by NSF award PHY-1429873, the Research Corporation for Science Advancement, and by Cal State Fullerton; and on the GPC supercomputer at the SciNet HPC Consortium [81]. SciNet is funded by: the Canada Foundation for Innovation under the auspices of Compute Canada; the Government of Ontario; Ontario Research Fund–Research Excellence; and the University of Toronto.

- [1] LIGO Scientific Collaboration, *Classical and Quantum Gravity* **32**, 074001 (2015).
- [2] G. M. Harry et al. (LIGO Scientific Collaboration), *Class.Quant.Grav.* **27**, 084006 (2010).
- [3] F. Acernese et al. (The Virgo Collaboration), “Advanced Virgo Baseline Design,” (2009), [Virgo Technical Document VIR-0027A-09].
- [4] K. Somiya (KAGRA Collaboration), *Class.Quant.Grav.* **29**, 124007 (2012), [arXiv:1111.7185 \[gr-qc\]](#).
- [5] J. Abadie et al. (LIGO Scientific Collaboration, Virgo Collaboration), *Class.Quant.Grav.* **27**, 173001 (2010), [arXiv:1003.2480 \[astro-ph.HE\]](#).
- [6] L. Gou, J. E. McClintock, M. J. Reid, J. A. Orosz, J. F. Steiner, R. Narayan, J. Xiang, R. A. Remillard, K. A. Arnaud, and S. W. Davis, *Astrophys. J.* **742**, 85 (2011), [arXiv:1106.3690 \[astro-ph.HE\]](#).
- [7] A. C. Fabian, D. R. Wilkins, J. M. Miller, R. C. Reis, C. S. Reynolds, E. M. Cackett, M. A. Nowak, G. G. Pooley, K. Pottschmidt, J. S. Sanders, R. R. Ross, and J. Wilms, *Monthly Notices of the Royal Astronomical Society* **424**, 217 (2012), [arXiv:1204.5854 \[astro-ph.HE\]](#).
- [8] L. Gou, J. E. McClintock, R. A. Remillard, J. F. Steiner, M. J. Reid, et al., (2013), [arXiv:1308.4760 \[astro-ph.HE\]](#).
- [9] J. M. Miller, C. S. Reynolds, A. C. Fabian, G. Miniutti, and L. C. Gallo, *Astrophys. J.* **697**, 900 (2009), [arXiv:0902.2840 \[astro-ph.HE\]](#).
- [10] J. E. McClintock, R. Shafee, R. Narayan, R. A. Remillard, S. W. Davis, et al., *Astrophys.J.* **652**, 518 (2006), [arXiv:astro-ph/0606076 \[astro-ph\]](#).
- [11] J. Miller, C. Reynolds, A. Fabian, G. Miniutti, and L. Gallo, *Astrophys.J.* **697**, 900 (2009), [arXiv:0902.2840 \[astro-ph.HE\]](#).
- [12] M. Agathos, W. Del Pozzo, T. G. F. Li, C. V. D. Broeck, J. Veitch, et al., *Phys.Rev.* **D89**, 082001 (2014), [arXiv:1311.0420 \[gr-qc\]](#).
- [13] W. D. Pozzo, K. Grover, I. Mandel, and A. Vecchio, *Class.Quant.Grav.* **31**, 205006 (2014), [arXiv:1408.2356 \[gr-qc\]](#).
- [14] I. Mandel, C.-J. Haster, M. Dominik, and K. Belczynski, “Distinguishing types of compact-object binaries using the gravitational-wave signatures of their mergers,” (2015).
- [15] M. Dominik, K. Belczynski, C. Fryer, D. E. Holz, E. Berti, et al., *Astrophys.J.* **779**, 72 (2013), [arXiv:1308.1546 \[astro-ph.HE\]](#).
- [16] C. L. Fryer, K. Belczynski, G. Wiktorowicz, M. Dominik, V. Kalogera, et al., *Astrophys.J.* **749**, 91 (2012), [arXiv:1110.1726 \[astro-ph.SR\]](#).
- [17] F. Pannarale and F. Ohme, (2014), [arXiv:1406.6057 \[gr-qc\]](#).
- [18] S. I. Blinnikov, I. D. Novikov, T. V. Perevodchikova, and A. G. Polnarev, *Soviet Astronomy Letters* **10**, 177 (1984).
- [19] B. Paczynski, *Astrophys.J.* **308**, L43 (1986).
- [20] D. Eichler, M. Livio, T. Piran, and D. N. Schramm, *Nature* **340**, 126 (1989).
- [21] F. Foucart, M. B. Deaton, M. D. Duez, L. E. Kidder, I. Macdonald, et al., *Phys.Rev.* **D87**, 084006 (2013), [arXiv:1212.4810 \[gr-qc\]](#).
- [22] G. Turin, *Information Theory, IRE Transactions on* **6**, 311 (1960).
- [23] C. Van Den Broeck, D. A. Brown, T. Cokelaer, I. Harry, G. Jones, et al., *Phys.Rev.* **D80**, 024009 (2009), [arXiv:0904.1715 \[gr-qc\]](#).
- [24] J. Abadie et al. (LIGO Scientific Collaboration, Virgo Collaboration), *Phys.Rev.* **D85**, 082002 (2012), [arXiv:1111.7314 \[gr-qc\]](#).
- [25] J. Abadie et al. (LIGO Scientific Collaboration, Virgo Collaboration), *Phys.Rev.* **D82**, 102001 (2010), [arXiv:1005.4655 \[gr-qc\]](#).
- [26] B. Abbott et al. (LIGO Scientific Collaboration), *Phys.Rev.* **D80**, 047101 (2009), [arXiv:0905.3710 \[gr-qc\]](#).
- [27] B. Abbott et al. (LIGO Scientific Collaboration), *Phys.Rev.* **D79**, 122001 (2009), [arXiv:0901.0302 \[gr-qc\]](#).
- [28] B. Abbott et al. (LIGO Scientific Collaboration), *Phys.Rev.* **D78**, 042002 (2008), [arXiv:0712.2050 \[gr-qc\]](#).
- [29] J. E. McClintock, R. Shafee, R. Narayan, R. A. Remillard, S. W. Davis, and L.-X. Li, *Astrophys. J.* **652**, 518 (2006).
- [30] L. Gou, J. E. McClintock, R. A. Remillard, J. F. Steiner, M. J. Reid, et al., *Astrophys.J.* **790**, 29 (2014).
- [31] J. E. McClintock, R. Narayan, and J. F. Steiner, *Space Sci.Rev.* **183**, 295 (2014), [arXiv:1303.1583 \[astro-ph.HE\]](#).
- [32] C. S. Reynolds, *Space Science Reviews* **183**, 277 (2014), [arXiv:1302.3260 \[astro-ph.HE\]](#).
- [33] I. Harry, A. Nitz, D. A. Brown, A. Lundgren, E. Ochsner, et al., (2013), [arXiv:1307.3562 \[gr-qc\]](#).
- [34] T. D. Canton, A. H. Nitz, A. P. Lundgren, A. B. Nielsen, D. A. Brown, et al., (2014), [arXiv:1405.6731 \[gr-qc\]](#).
- [35] L. Blanchet, *Living Rev.Rel.* **9**, 4 (2006).
- [36] A. Taracchini, Y. Pan, A. Buonanno, E. Barausse, M. Boyle, et al., *Phys.Rev.* **D86**, 024011 (2012), [arXiv:1202.0790 \[gr-qc\]](#).
- [37] A. H. Nitz, A. Lundgren, D. A. Brown, E. Ochsner, D. Keppel, et al., (2013), [arXiv:1307.1757 \[gr-qc\]](#).
- [38] A. Boh, S. Marsat, and L. Blanchet, *Class.Quant.Grav.* **30**, 135009 (2013), [arXiv:1303.7412 \[gr-qc\]](#).
- [39] L. Blanchet, A. Buonanno, and G. Faye, *Phys.Rev.* **D84**, 064041 (2011), [arXiv:1104.5659 \[gr-qc\]](#).
- [40] L. Santamaria, F. Ohme, P. Ajith, B. Bruegmann, N. Dorband, et al., *Phys.Rev.* **D82**, 064016 (2010), [arXiv:1005.3306 \[gr-qc\]](#).
- [41] LIGO (David Shoemaker), Advanced LIGO anticipated sensitivity curves, Tech. Rep. (LIGO Document T0900288-v3, 2009).
- [42] B. Kiziltan, A. Kottas, M. De Yoreo, and S. E. Thorsett, *The Astrophysical Journal* **778**, 66 (2013), [arXiv:1011.4291 \[astro-ph.GA\]](#).
- [43] D. R. Lorimer, M. Bailes, R. J. Dewey, and P. A. Harrison, *Monthly Notices of the Royal Astronomical Society* **263**, 403 (1993).
- [44] K. A. Postnov and L. R. Yungelson, *Living Rev.Rel.* **17**, 3 (2014), [arXiv:1403.4754 \[astro-ph.HE\]](#).
- [45] J. S. Read, L. Baiotti, J. D. E. Creighton, J. L. Friedman, B. Giacomazzo, et al., *Phys.Rev.* **D88**, 044042 (2013), [arXiv:1306.4065 \[gr-qc\]](#).
- [46] B. D. Lackey, K. Kyutoku, M. Shibata, P. R. Brady, and J. L. Friedman, *Phys.Rev.* **D89**, 043009 (2014), [arXiv:1303.6298 \[gr-qc\]](#).
- [47] F. Foucart, M. B. Deaton, M. D. Duez, E. O’Connor, C. D. Ott, et al., *Phys.Rev.* **D90**, 024026 (2014), [arXiv:1405.1121 \[astro-ph.HE\]](#).
- [48] S. Waldman (the LIGO Scientific Collaboration), (2011), [arXiv:1103.2728 \[gr-qc\]](#).
- [49] L. Lindblom, B. J. Owen, and D. A. Brown, *Phys.Rev.* **D78**, 124020 (2008), [arXiv:0809.3844 \[gr-qc\]](#).
- [50] <http://www.black-holes.org/SpEC.html>.
- [51] B. Szilagyi, J. Blackman, A. Buonanno, A. Taracchini, H. P. Pfeiffer, et al., (2015), [arXiv:1502.04953 \[gr-qc\]](#).
- [52] C. O. Lousto and J. Healy, (2015), [arXiv:1506.04768 \[gr-qc\]](#).
- [53] <http://www.black-holes.org/waveforms/>.

- [54] B. Szilgyi, *Int.J.Mod.Phys.* **D23**, 1430014 (2014), [arXiv:1405.3693 \[gr-qc\]](#).
- [55] P. Ajith, M. Hannam, S. Husa, Y. Chen, B. Bruegmann, et al., *Phys.Rev.Lett.* **106**, 241101 (2011), [arXiv:0909.2867 \[gr-qc\]](#).
- [56] B. Sathyaprakash and S. Dhurandhar, *Phys.Rev.* **D44**, 3819 (1991).
- [57] C. Cutler and E. E. Flanagan, *Phys.Rev.* **D49**, 2658 (1994), [arXiv:gr-qc/9402014 \[gr-qc\]](#).
- [58] S. Droz, D. J. Knapp, E. Poisson, and B. J. Owen, *Phys.Rev.* **D59**, 124016 (1999), [arXiv:gr-qc/9901076 \[gr-qc\]](#).
- [59] L. Blanchet, T. Damour, G. Esposito-Farese, and B. R. Iyer, *Phys.Rev.Lett.* **93**, 091101 (2004), [arXiv:gr-qc/0406012 \[gr-qc\]](#).
- [60] L. Blanchet and B. R. Iyer, *Phys.Rev.* **D71**, 024004 (2005), [arXiv:gr-qc/0409094 \[gr-qc\]](#).
- [61] P. Jaranowski and G. Schaefer, *Annalen Phys.* **9**, 378 (2000), [arXiv:gr-qc/0003054 \[gr-qc\]](#).
- [62] P. Jaranowski and G. Schaefer, *Phys.Rev.* **D60**, 124003 (1999), [arXiv:gr-qc/9906092 \[gr-qc\]](#).
- [63] T. Damour, P. Jaranowski, and G. Schaefer, *Phys.Lett.* **B513**, 147 (2001), [arXiv:gr-qc/0105038 \[gr-qc\]](#).
- [64] L. Blanchet, G. Faye, B. R. Iyer, and S. Sinha, *Class.Quant.Grav.* **25**, 165003 (2008), 57 pages, no figures, [arXiv:0802.1249 \[gr-qc\]](#).
- [65] L. Blanchet, A. Buonanno, and G. Faye, (2012), [arXiv:1210.0764 \[gr-qc\]](#).
- [66] A. Bohe, S. Marsat, G. Faye, and L. Blanchet, *Class.Quant.Grav.* **30**, 075017 (2013), [arXiv:1212.5520](#).
- [67] A. Taracchini, A. Buonanno, Y. Pan, T. Hinderer, M. Boyle, et al., *Phys.Rev.* **D89**, 061502 (2014), [arXiv:1311.2544 \[gr-qc\]](#).
- [68] A. Buonanno, Y. Pan, H. P. Pfeiffer, M. A. Scheel, L. T. Buchman, and L. E. Kidder, *Phys. Rev. D* **79**, 124028 (2009), [arXiv:0902.0790 \[gr-qc\]](#).
- [69] “LSC Algorithm Library,” <https://www.lsc-group.phys.uwm.edu/daswg/projects/lalsuite.html>.
- [70] K. Alvi, *Phys.Rev.* **D64**, 104020 (2001), [arXiv:gr-qc/0107080 \[gr-qc\]](#).
- [71] H. Wilbraham, *Cambridge and Dublin Mathematical Journal* **III**, 198 (1848).
- [72] B. Bruegmann, J. A. Gonzalez, M. Hannam, S. Husa, U. Sperhake, et al., *Phys.Rev.* **D77**, 024027 (2008), [arXiv:gr-qc/0610128 \[gr-qc\]](#).
- [73] S. Husa, M. Hannam, J. A. Gonzalez, U. Sperhake, and B. Bruegmann, *Phys.Rev.* **D77**, 044037 (2008), [arXiv:0706.0904 \[gr-qc\]](#).
- [74] I. MacDonald, A. H. Mroue, H. P. Pfeiffer, M. Boyle, L. E. Kidder, et al., *Phys.Rev.* **D87**, 024009 (2013), [arXiv:1210.3007 \[gr-qc\]](#).
- [75] S. Husa, “Private communication.” (2015).
- [76] P. Kumar, I. MacDonald, D. A. Brown, H. P. Pfeiffer, K. Cannon, et al., *Phys.Rev.* **D89**, 042002 (2014), [arXiv:1310.7949 \[gr-qc\]](#).
- [77] A. H. Mroue, M. A. Scheel, B. Szilgyi, H. P. Pfeiffer, M. Boyle, et al., (2013), [arXiv:1304.6077 \[gr-qc\]](#).
- [78] M. Prer, *Class.Quant.Grav.* **31**, 195010 (2014), [arXiv:1402.4146 \[gr-qc\]](#).
- [79] S. Khan, “Phenomd (NRDA 2013),” [http://www.grg.uib.es/NRDA13/slides/Szilgyi\\_StretchingTheLimitsOfNR.pdf](http://www.grg.uib.es/NRDA13/slides/Szilgyi_StretchingTheLimitsOfNR.pdf).
- [80] F. Ohme, A. B. Nielsen, D. Keppel, and A. Lundgren, *Phys.Rev.* **D88**, 042002 (2013), [arXiv:1304.7017 \[gr-qc\]](#).
- [81] C. Loken, D. Gruner, L. Groer, R. Peltier, N. Bunn, M. Craig, T. Henriques, J. Dempsey, C.-H. Yu, J. Chen, L. J. Dursi, J. Chong, S. Northrup, J. Pinto, N. Knecht, and R. V. Zon, *J. Phys.: Conf. Ser.* **256**, 012026 (2010).